Antarctic surface temperature and elevation during the Last Glacial Maximum

Christo Buizert, T. Fudge, William Roberts, Eric Steig, Sam Sherriff-Tadano, Catherine Ritz, Eric Lefebvre, Jon Edwards, Kenji Kawamura, Ikumi Oyabu, et al.

Antarctic surface temperature and elevation during the Last Glacial Maximum

Authors: Christo Buizert[1*], T.J. Fudge[2], William H. G. Roberts[3], Eric J. Steig[2], Sam Sherriff-Tadano[4], Catherine Ritz[5], Eric Lefebvre[5], Jon Edwards[1], Kenji Kawamura[6], Ikumi Oyabu[6], Hideaki Motoyama[6], Emma C. Kahle[2], Tyler R. Jones[7], Ayako Abe-Ouchi[4], Takashi Obase[4], Carlos Martin[8], Hugh Corr[8], Jeffrey P. Severinghaus[9], Ross Beaudette[9], Jenna A. Epifanio[1], Edward J. Brook[1], Kaden Martin[1], Jérôme Chappellaz[10], Shuji Aoki[11], Takakiyo Nakazawa[11], Todd A. Sowers[12], Richard B. Alley[12], Jinho Ahn[13], Michael Sigl[14], Mirko Severi[15], Nelia W. Dunbar[16], Anders Svensson[17], John Fegyveresi[18], Chengfei He[19], Zhengyu Liu[19], Jiang Zhu[20], Bette Otto-Bliesner[20], Vladimir Y. Lipenkov[21], Masa Kageyama[22], and Jakob Schwander[14]

[1]College of Earth Ocean and Atmospheric Sciences, Oregon State University, Corvallis OR 97331, USA

[2]Department of Earth and Space Science, University of Washington, Seattle WA 98195, USA

[3]Geographical and Environmental Sciences, Northumbria University, Newcastle, UK

[4]Atmosphere and Ocean Research Institute, The University of Tokyo, Kashiwa 277-8568, Japan

[5]Université Grenoble Alpes, CNRS, IRD, IGE, Grenoble, France

[6]National Institute for Polar Research, Tachikawa, Tokyo, Japan

[7]Institute of Arctic and Alpine Research, University of Colorado, Boulder CO 80309, USA

[8]British Antarctic Survey, Cambridge, UK

[9]Scripps Institution of Oceanography, University of California San Diego, La Jolla CA 92093 , USA

[10]Univ. Grenoble Alpes, CNRS, IRD, Grenoble INP, IGE, 38000 Grenoble, France

[11]Center for Atmospheric and Oceanic Studies, Graduate School of Science, Tohoku University, Sendai 980-8578, Japan

[12]The Earth and Environmental Systems Institute, Pennsylvania State University, University Park, PA 16802, USA

[13]School of Earth and Environmental Sciences, Seoul National University, Seoul 08826, South Korea

[14]Climate and Environmental Physics, Physics Institute & Oeschger Center for Climate Change Research, University of Bern, Sidlerstrasse 5, 3012 Bern, Switzerland

[15]Department of Chemistry "Ugo Schiff", University of Florence, Florence, Italy

[16]New Mexico Bureau of Geology & Mineral Resources, Earth and Environmental Science Department, New Mexico Tech, Socorro, NM 87801, USA

[17]Niels Bohr Institute, University of Copenhagen, Copenhagen, Denmark

[18]School of Earth and Sustainability, North Arizona University, Flagstaff, AZ 86011, USA

[19]Department of Geography, Ohio State University, Columbus, OH 43210, USA

[20]National Center for Atmospheric Research, Boulder CO 80307, USA

[21]Climate and Environmental Research Laboratory, Arctic and Antarctic Research Institute, St. Petersburg, 199397, Russia

[22]Laboratoire des Sciences du Climat et de l'Environnement-IPSL, Université Paris-Saclay, Gif-sur-Yvette, France

*Correspondence to: christo.buizert@oregonstate.edu

Abstract: Water stable isotopes in polar ice cores are a widely used temperature proxy in paleoclimate reconstruction, yet calibration remains challenging in East Antarctica. Here we reconstruct the magnitude and spatial pattern of Last Glacial Maximum surface cooling in Antarctica using borehole thermometry and firn properties in seven ice cores. West Antarctic sites cooled ~10ºC relative to preindustrial. East Antarctic sites show a range from ~4 to ~7°C cooling, consistent with results of global climate models when the effects of topographic changes indicated by ice-core air-content data are included, but less than indicated by use of water stable isotopes calibrated against modern spatial gradients. An altered Antarctic temperature inversion during the glacial reconciles our estimates with water isotope observations.

One Sentence Summary: Temperature reconstructions based on borehole thermometry and firn properties, suggest that interpretation of ice core water isotopes using modern spatial slopes overestimates last glacial maximum surface cooling in central East Antarctica.

Main Text:

Using oxygen and hydrogen isotope ratios in ancient polar ice as records of past site temperature requires a calibration (*1*). Surface temperature and isotopic composition of precipitation correlate spatially in Antarctica, with a regression coefficient α_S (spatial slope) of 0.80 ‰K^{-1} for $\delta^{18}O$ (*2*). Reconstructing past temperatures requires regression over time, and this temporal slope α_T may differ from α_S. In East Antarctica where the longest continuous ice core records, going back to 800 ka BP (thousands of years before present), have been extracted (*3*), independent temperature estimates are not available and the spatial slope is commonly used to convert isotopic ratios to temperature (*1*); this approach gives a surface temperature difference ΔT_S between the Last Glacial Maximum (LGM, 26-18 ka BP) and preindustrial of around -9°C (*1, 4, 5*).

Antarctic LGM-preindustrial isotope changes depend on many factors including hemispheric sea-surface temperatures (*6*), sea ice extent (*7*), ice sheet elevation (*8*), vapor origin and transport, precipitation seasonality, and post-depositional isotopic exchange (*9*). Isotope-enabled general circulation models seek to capture these physical processes, making them an invaluable tool for studying isotopic variations. Such models simulate LGM-preindustrial α_T ranging from 0.3 to 1.4 ‰K^{-1} in central East Antarctica (implied ΔT_S of 4 to 20°C), implying several aforementioned processes are poorly constrained (*8, 10-12*).

We distinguish three temperatures: (i) the climatic temperature T_{CLIM} at constant elevation (relative to the present-day geoid); (ii) the surface temperature T_S, which may differ from the climatic temperature due to changing ice sheet topography; and (iii) the vapor condensation temperature T_C, which is warmer than the surface due to the strong Antarctic inversion (*2, 13*).

Here, we empirically reconstruct LGM surface temperature across Antarctica (Fig. 1) using two independent methods. We investigate five East Antarctic ice cores: EPICA (European Project for Ice Coring in Antarctica) Dome C (EDC), EPICA Dronning Maud Land (EDML), Dome Fuji (DF), Talos Dome (TAL), and South Pole (SP); and two West Antarctic cores: West Antarctic Ice Sheet (WAIS) Divide (WD), and Siple Dome (SDM).

First, we estimate ΔT_S at EDC and DF from the measured borehole temperature profiles (Fig. 2) using a method similar to that employed recently at WD (*14*). Due to the downward ice flow and low thermal diffusivity, the ice sheet maintains an imprint of its past surface temperature history. The large ice sheet thickness at EDC and DF is favorable for preserving past temperatures, yet the low accumulation rate is not. Consequently, the relative uncertainty in the EDC and DF borehole reconstructions is larger than that at WD. To constrain the problem better we use downward ice

velocities measured via phase-sensitive radio echo sounding (EDC only), and accurate age constraints derived via volcanic synchronization to the layer-counted WD timescale.

We force a 1-D heat transport-ice flow model at the surface boundary with a temperature history based on the $\delta^{18}O$ record scaled with a constant α_T value (*10*). Applying traditional isotope scaling ($\alpha_T \approx 0.7$ ‰ K^{-1}, yielding ΔT_S = -9ºC at EDC and -7.5ºC at DF) simulates temperature profiles that do not fit the borehole observations at either site (Fig. 2). At EDC the model-data fit is optimized for α_T = 1.14 ‰ K^{-1} consistent with ΔT_S = -5.5ºC (95% confidence range is -6.9 ºC to -3.1ºC). At DF the optimal ΔT_S is in the -2.0 ºC to -5.4 ºC range; we provide a range without a best estimate because at DF there are no direct constraints on the downward ice velocity. In Fig. 1 the WD, EDC and DF borehole estimates are marked "BH".

Second, we reconstruct past climate at all seven sites using the dependence of firn densification, the gradual transformation of polar snow to ice, on T_S and accumulation rate (A). Air bubbles are isolated from the atmosphere at the lock-in depth (50-120 m below the surface), an event preserved in two ice core signals (*15*): $\delta^{15}N$ of N_2 which records past firn column thickness via gravitational enrichment, and the gas age-ice age difference or Δage. Critically, the $\delta^{15}N$ and Δage-isopleths are perpendicular in T_S-A space (Fig. 3A), meaning that if $\delta^{15}N$ and Δage are independently known, a unique climatic [T_S, A] solution exists (subject to the uncertainties of the firn model).

Synchronization using both volcanic deposits and globally synchronous abrupt atmospheric methane variations, allows us to estimate Δage empirically for the Antarctic ice cores (*10, 16*). We use an inverse dynamical firn densification-heat transport model (*17, 18*) to reconstruct T_S and A histories that optimize the fit to Δage and $\delta^{15}N$ data (Fig. 3B-C). Reconstructed accumulation rates agree (within uncertainty) with independent estimates (Fig. S8). Methodological biases and

111 uncertainties are estimated using a Monte-Carlo approach (*10*). The histograms in Fig.1 give the
112 ΔT_S distribution of the Δage-based reconstruction.

113 In East Antarctica, ΔT_S ranges from -3.8±2.0°C (DF) to -7.1±1.7°C (TAL); at DF, EDC and EDML,
114 ΔT_S is substantially lower than estimates from isotope scaling using α_S. The two West Antarctic
115 sites have similar ΔT_S of -10.2±2.4°C (SDM) to -10.3±1.3°C (WD). The Δage- and borehole-based
116 reconstruction methods agree within uncertainty at all sites (Fig. 1). Allowing for more flank-like
117 ice flow at EDC during the glacial period (which would occur if the divide position were different
118 than at present), improves the agreement by changing the borehole estimate to around -4.5ºC (*10*);
119 we choose to report the -5.5ºC value to keep both methods independent. PMIP4 (Paleoclimate
120 Modeling Intercomparison Project phase 4) simulations (*19*) find a seven-site-mean ΔT_S
121 magnitude that is 1.2 ± 4.6ºC larger than our Δage-based reconstructions (mean and spread of ten
122 climate models; Fig. 1).

123 We emphasize that the firn method is primarily constrained by the empirical Δage estimates.
124 Because T_S and A broadly co-vary via the saturation vapor pressure, the deglacial climatic changes
125 run parallel to the $\delta^{15}N$-isopleths (Fig. 3A). Therefore, $\delta^{15}N$ data alone do not constrain the
126 magnitude of climate change meaningfully. The effects of T_S and A are additive in Δage, however,
127 making Δage a sensitive proxy for climate change (Fig. 3D), as first noted by Jakob Schwander
128 (*20*). The empirical Δage at 24ka is larger than at 18 ka BP for all five cores where both are
129 available, and coldest conditions in Antarctica occur around 27-24 ka BP in our reconstructions
130 (Fig. S8h); this follows expectations from local insolation (*21*).

We propose that elevation changes explain the spatial differences in ΔT_S (*8*). Let Δz be the LGM elevation anomaly relative to present. We present new WD and DF total air content data (Fig. S12), and interpret them in terms of elevation change (*22*). These data suggest a 420 m (range: 280 – 590 m) contrast in Δz between WD and central East Antarctica (here DF and EDC) – for example $\Delta z = +300$ m at WAIS and $\Delta z = -120$ m in central East Antarctica (Fig. 4B). Our estimate is broadly in agreement with LGM ice sheet reconstructions that suggest a West-East Δz contrast between 160 and 560 m (*10*). Although the implied Δz at WAIS exceeds the observed highstand at ice margin nunataks (*23*), such data do not strongly constrain the elevation at WD over 500 km away. The corresponding ΔT_S contrast (WD ΔT_S minus the average ΔT_S at DF and EDC) is -6.2 ± 2.3ºC in the Δage-based reconstructions, -6.0 ± 2.0ºC in the borehole reconstructions, and -5.9 ± 2.7ºC in the PMIP4 model ensemble; the level of agreement suggests this is a robust feature of Antarctic LGM climate. This temperature contrast is thus plausibly linked to Δz via the (spatial) lapse rate in interior of Antarctica of around -12ºC km^{-1} (*2, 24*).

To further assess the elevation impact on ΔT_S we perform an atmosphere-ocean general circulation model (AOGCM) sensitivity study of Antarctic LGM climate using the MIROC and HadCM3 models and a series of LGM topographic reconstructions (*10*). We first estimate climatic LGM cooling using full LGM boundary conditions (including LGM albedo) but preindustrial Antarctic topography; this yields a seven-site average ΔT_{CLIM} of -4.7ºC and -7.0ºC in the MIROC and HadCM3 models respectively, but stronger albedo-driven cooling is found over the Ross and Weddell Seas due to ice growth onto the continental shelf (Fig. 4A). Note that simulated climatic ΔT_{CLIM} is similar in interior West and East Antarctica in the absence of topographic change.

Next, we perform climate simulations with five Antarctic LGM topographic reconstructions. These reconstructions suggest Δz of +100 to +600 m in interior WAIS and down to -250 m in interior East Antarctica (Fig. 4B). These changes result in greater ΔT_S in West than in central East Antarctica (Fig. 4C), in agreement with our reconstructions. By comparing the various topographic reconstructions, we find that ΔT_S is closely linked to Δz in both models following the dry adiabatic lapse rate of -9.8°C km^{-1} (Fig. 4D). There is also a fraction of the variance that cannot be explained by lapse rate effects that is due to the topography altering the atmospheric circulation around Antarctica. We find a correlation $r = 0.96$ between the reconstructed and the simulated site ΔT_S pattern (averaged across the five topographic reconstructions and both models); for the PMIP4 multi-model mean this correlation is $r = 0.95$. We conclude that LGM ice sheet topography change plausibly explains the ΔT_S spatial variability in our reconstruction (*8*).

Our findings have implications for the interpretation of water isotopes in Antarctic ice cores. We find α_T in the range of 0.9 to 1.4 ‰K^{-1} in East Antarctica and therefore $\alpha_T > \alpha_S$, opposite to Greenland where $\alpha_T < \alpha_S$ (*17, 25*). We compare our α_T with those from LGM and preindustrial simulations using the latest generation isotope-enabled Community Earth System Model (iCESM, Fig. 4E). The good agreement ($r = 0.91$; 0.06 ‰ K^{-1} mean offset) demonstrates our reconstructed α_T are consistent with isotope physics, yet the large inter-model spread in simulated α_T (see section S3.5 in (*10*) for a review) prevents us from claiming it validates our results. While the α_T agree well, iCESM simulates a ΔT_S and LGM-preindustrial $\delta^{18}O$ change that are both too large (compared to our reconstructions and ice core data, respectively).

Last, we investigate changes to the strong surface-based inversion in the Antarctic boundary layer (Fig. 4F). The condensation temperature T_C is higher than T_S, and they correlate spatially with a

slope dT_C/dT_S in the 0.63-0.67 range (*2, 13, 26*). T_C controls precipitation $\delta^{18}O$, with a present-day spatial sensitivity of $d\delta^{18}O/dT_C = d\delta^{18}O/dT_S \times dT_S/dT_C \approx 0.80/0.65 = 1.23$ ‰ K^{-1}. We now assume that, unlike ΔT_S, the LGM-preindustrial change ΔT_C can be estimated using this spatial slope via $\Delta T_C = \Delta\delta^{18}O/1.23$ (Fig. 4F). At WD and SDM the $\alpha_T \approx \alpha_S$ assumption holds, suggesting the ratio $\Delta T_C/\Delta T_S$ is close to the present-day ratio of 0.65; in central East Antarctica the ratio $\Delta T_C/\Delta T_S$ exceeds 0.65 consistent with $\alpha_T > \alpha_S$. We plotted simulated ΔT_S vs. ΔT_C across interior Antarctica from a wide range of AOGCMs and topographies; we find the ratio $\Delta T_C/\Delta T_S$ ranges from 0.48 to 1.3 (95% interval, grey lines) with our empirical reconstructions falling within the model data cloud (Fig. 4F). In aggregate these simulations find that $\Delta T_C/\Delta T_S$ tends to exceed the present-day ratio of 0.65 (~79% of model data points) – such a change to the inversion structure would result in $\alpha_T > \alpha_S$ for ΔT_S. In the iCESM simulations the $\Delta T_C/\Delta T_S$ and α_T fields look similar, with the $\Delta T_C/\Delta T_S = 0.65$ contour line broadly aligning with the $\alpha_T = 0.8$ ‰K^{-1} contour line (Fig. S11). We conclude that physically plausible changes to the inversion (*27, 28*) may reconcile our reconstructions with previous work on Antarctic LGM water isotopes.

Our reconstructions improve the LGM Antarctic temperature estimation and provide a benchmark for testing the ability of (isotope-enabled) climate models to simulate climate states radically different from the late Holocene. For surface temperature, the spatial isotopic slope is not always a good approximation of the temporal slope, challenging the prevalent interpretation of ice core water isotopes in Antarctica.

References and Notes:

1. J. Jouzel *et al.*, Magnitude of isotope/temperature scaling for interpretation of central Antarctic ice cores. *J. Geophys. Res.* **108**, 4361 (2003).
2. V. Masson-Delmotte *et al.*, A Review of Antarctic Surface Snow Isotopic Composition: Observations, Atmospheric Circulation, and Isotopic Modeling. *J. Clim.* **21**, 3359-3387 (2008).
3. EPICA-Community-Members, Eight glacial cycles from an Antarctic ice core. *Nature* **429**, 623-628 (2004).
4. V. Masson-Delmotte *et al.*, EPICA Dome C record of glacial and interglacial intensities. *Quat. Sci. Rev.* **29**, 113-128 (2010).
5. J. Jouzel *et al.*, Orbital and millennial Antarctic climate variability over the past 800,000 years. *Science* **317**, 793-796 (2007).
6. C. Risi, S. Bony, F. Vimeux, J. Jouzel, Water-stable isotopes in the LMDZ4 general circulation model: Model evaluation for present-day and past climates and applications to climatic interpretations of tropical isotopic records. *J. Geophys. Res.* **115**, (2010).
7. D. Noone, I. Simmonds, Sea ice control of water isotope transport to Antarctica and implications for ice core interpretation. *Journal of Geophysical Research: Atmospheres (1984–2012)* **109**, (2004).
8. M. Werner, J. Jouzel, V. Masson-Delmotte, G. Lohmann, Reconciling glacial Antarctic water stable isotopes with ice sheet topography and the isotopic paleothermometer. *Nature Communications* **9**, 3537 (2018).
9. M. Casado *et al.*, Archival of the water stable isotope signal in East Antarctic ice cores. *The Cryosphere Discuss.* **2016**, 1-33 (2016).
10. Materials and methods are available as supplementary materials on Science Online.
11. J.-E. Lee, I. Fung, D. J. DePaolo, B. Otto-Bliesner, Water isotopes during the Last Glacial Maximum: New general circulation model calculations. *J. Geophys. Res.* **113**, (2008).
12. G. Hoffmann, J. Jouzel, V. Masson, Stable water isotopes in atmospheric general circulation models. *Hydrological Processes* **14**, 1385-1406 (2000).
13. J. Jouzel, L. Merlivat, Deuterium and oxygen 18 in precipitation: Modeling of the isotopic effects during snow formation. *J. Geophys. Res.* **89**, 11749-11757 (1984).
14. K. M. Cuffey *et al.*, Deglacial temperature history of West Antarctica. *Proc. Natl. Acad. Sci. U. S. A.*, (2016).
15. T. Sowers, M. Bender, D. Raynaud, Y. S. Korotkevich, δ15N of N2 in air trapped in polar ice: A tracer of gas transport in the firn and a possible constraint on ice age-gas age differences. *J. Geophys. Res.* **97**, 15683-15697 (1992).
16. J. A. Epifanio *et al.*, The SP19 chronology for the South Pole Ice Core - Part 2: gas chronology, delta age, and smoothing of atmospheric records. *Clim. Past* **2020**, 2431–2444 (2020).
17. C. Buizert *et al.*, Greenland temperature response to climate forcing during the last deglaciation. *Science* **345**, 1177-1180 (2014).
18. M. M. Herron, C. C. Langway, Firn densification: An empirical model. *J. Glaciol.* **25**, 373-385 (1980).
19. M. Kageyama *et al.*, The PMIP4 contribution to CMIP6-Part 4: Scientific objectives and experimental design of the PMIP4-CMIP6 Last Glacial Maximum experiments and PMIP4 sensitivity experiments. *Geoscientific Model Development* **10**, 4035-4055 (2017).
20. J. Schwander *et al.*, Age scale of the air in the summit ice: Implication for glacial-interglacial temperature change. *J. Geophys. Res.* **102**, 19483-19493 (1997).
21. P. Huybers, G. Denton, Antarctic temperature at orbital timescales controlled by local summer duration. *Nature Geosci* **1**, 787-792 (2008).
22. D. Raynaud *et al.*, The local insolation signature of air content in Antarctic ice. A new step toward an absolute dating of ice records. *Earth Planet. Sci. Lett.* **261**, 337-349 (2007).
23. P. Spector, J. Stone, B. Goehring, Thickness of the divide and flank of the West Antarctic Ice Sheet through the last deglaciation. *The Cryosphere* **13**, 3061-3075 (2019).
24. J. Fortuin, J. Oerlemans, Parameterization of the annual surface temperature and mass balance of Antarctica. *Ann. Glaciol* **14**, 78-84 (1990).
25. K. M. Cuffey *et al.*, Large Arctic Temperature Change at the Wisconsin-Holocene Glacial Transition. *Science* **270**, 455-458 (1995).

26. W. Connolley, The Antarctic temperature inversion. *International Journal of Climatology: A Journal of the Royal Meteorological Society* **16**, 1333-1342 (1996).
27. G. Krinner, C. Genthon, GCM simulations of the Last Glacial Maximum surface climate of Greenland and Antarctica. *Clim. Dyn.* **14**, 741-758 (1998).
28. N. P. Van Lipzig, E. Van Meijgaard, J. Oerlemans, The effect of temporal variations in the surface mass balance and temperature-inversion strength on the interpretation of ice-core signals. *J. Glaciol.* **48**, 611-621 (2002).
29. L. Tarasov, A. S. Dyke, R. M. Neal, W. R. Peltier, A data-calibrated distribution of deglacial chronologies for the North American ice complex from glaciological modeling. *Earth Planet. Sci. Lett.* **315–316**, 30-40 (2012).
30. C. Buizert *et al.*, The WAIS Divide deep ice core WD2014 chronology - part 1: Methane synchronization (68-31 ka BP) and the gas age-ice age difference. *Climate of the Past* **11**, 153-173 (2015).
31. M. Sigl *et al.*, The WAIS Divide deep ice core WD2014 chronology – Part 2: Annual-layer counting (0–31 ka BP). *Clim. Past* **12**, 769-786 (2016).

Acknowledgments: The idea of weak East Antarctic LGM cooling was suggested a decade ago by Sigfús J. Johnsen (1940–2013) and Jakob Schwander, but never published. We thank Emilie Capron and Amaëlle Landais for help in gathering $\delta^{15}N$ data; Takeo Hondoh and Takao Kameda for support in Dome Fuji air content analyses; Camille Bréant for sharing model output; Vasileios Gkinis for useful discussions; Wing-Le Chan for assistance with model analysis; Jean-Yves Peterschmitt for compiling PMIP4 model data, and all PMIP4 groups for sharing model output; Chris Adams of Corvidopolis for providing a toddler-free workspace during the COVID-19 pandemic.

Funding: This work was supported by the US National Science Foundation (NSF) through grants 1643394 (to C.B.), 1643355 (to T.J.F. and E.J.S), 1443472, 1643722 (to E.J.B), and 1738934 (to R.B.A.); the University of Washington Royalty Research Fund (to T.J.F); MEXT and the Japan Society for the Promotion of Science KAKENHI Grant Numbers 18749002, 26241011, 15KK0027, 17H06316 and 20H00639 (to K.K), 20H04327 (to I.O.), 22310003 (to T.N.), 15J12515, 17H06104, 17H06323 and 20K14552 (to A.A-O); the National Research Foundation of Korea (NRF) through grants NRF-2018R1A2B3003256 and NRF-2018R1A5A1024958 (to

277 J.A.); the European Research Council (ERC) under the European Union's Horizon 2020 research
278 and innovation programme through grant agreement No 820047 (to M.Si.); IT-MIUR-PNRA
279 (Italian Antarctic Research Program) through the BE-OI (PNRA16_00124) project (to M.Se.); the
280 Villum Investigator Project IceFlow (NR. 16572, to A.S.); Beyond EPICA - Oldest Ice Core EU
281 Coordination and Support Action; measurements at EDC (Concordia Station) were supported by
282 the French Polar Institute (IPEV, prog 902) and the Italian Antarctic Program (PNRA and ENEA).

283 **Author Contributions:** C.B., E.J.S., and W.H.G.R. conceived of the study; Δage-based
284 reconstructions by C.B.; ice flow and borehole temperature modeling by T.J.F. and C.R.; GCM
285 modeling by W.H.G.R., S.S.-T., T.O., A.A.-O., C.H., Z.L., J.Z., and B.O.-B..; PMIP4 model
286 compilation by M.K.; methane data by E.J.B., J.E., J.A., K.M., J.C., T.A.S., K.K., S.A. and T.N.;
287 $\delta^{15}N\text{-}N_2$ data by I.O., K.K., R.B., J.P.S., S.A. and T.N.; borehole thermometry data by C.R., E.L.
288 and H.M.; ApRES data by C.M. and H.C.; SP isotope data by E.J.S., E.C.K. and T.R.J.; air content
289 data and corrections by J.E., K.K., V.L., J.F. and R.B.A.; SDM chronology by T.J.F. and C.B.;
290 SDM tephra matches by N.W.D.; volcanic matching by M.Si., M.Se., A.S., T.J.F. and C.B.; J.Sc.
291 (and S.J.J.) independently performed a similar study that reached the same conclusion around a
292 decade ago; all authors contributed towards the final manuscript.

293 **Competing interests:** The authors declare no competing financial interests.

294 **Data and materials availability:** All new ice core data from this study are available in the
295 supplementary material data sheet and online at https://www.ncdc.noaa.gov/paleo/study/32632;
296 previously published data are available with their original publications and/or in publicly
297 accessible online data archives.

298

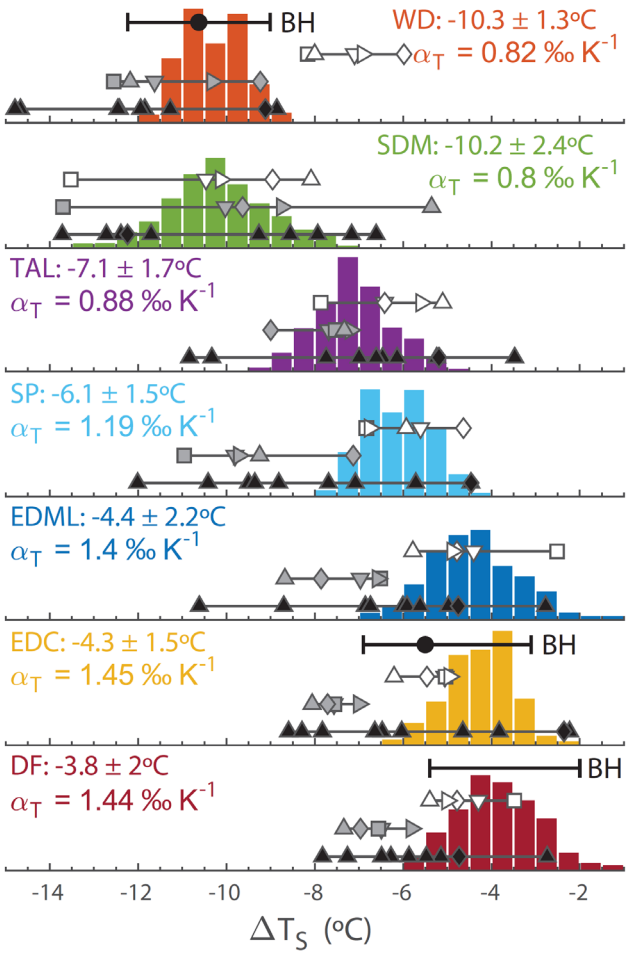

299

300 **Figure 1**. **Summary of Antarctic LGM cooling estimates**. Black markers with horizontal
301 errorbars marked "BH" give borehole estimates; WD results from ref. (*14*). Histograms give
302 distribution of Δage-based temperature reconstructions from a Monte Carlo sampling (N = 1000)
303 of model parameters; listed are mean and 2σ standard deviation of the distribution, as well as the
304 implied temporal isotope slope α_T. ΔT_S is the LGM (18-21.4 ka BP) minus preindustrial (0.5-2.5
305 ka BP) condition. White (MIROC), grey (HadCM3) and black (PMIP4) show AOGCM-simulated
306 ΔT_S, with symbols denoting different LGM topography reconstructions (*10*): Pollard and Deconto
307 2009 (downward triangle); Whitehouse et al. 2012 (square); Glac-1D (diamond, (*29*)); Golledge
308 et al. 2014 (rightward triangle); Ice-6G (upward triangle).

309

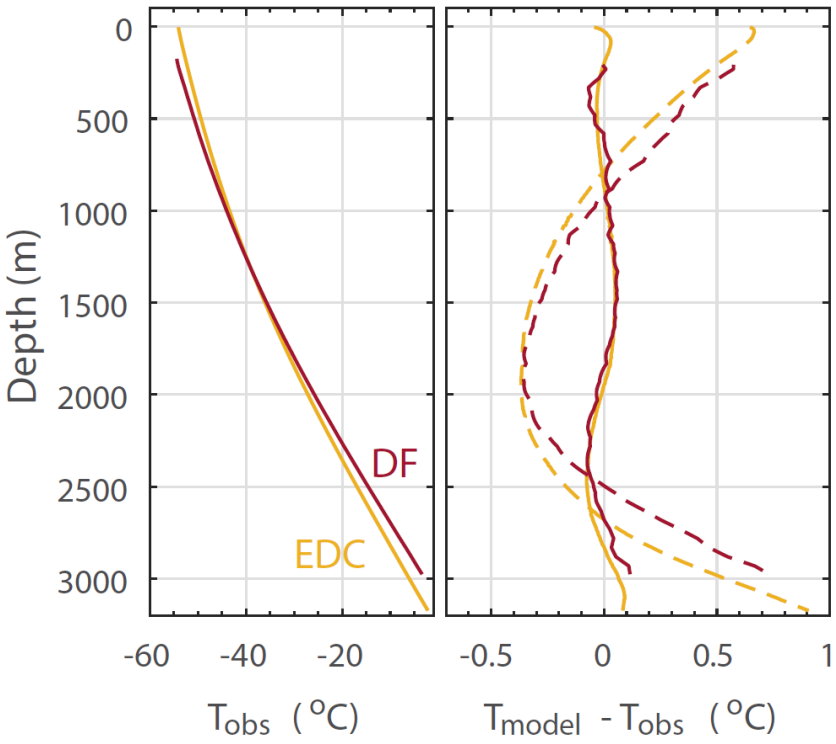

Figure 2. Borehole temperature reconstruction for EDC and DF. Left panel: Site borehole temperature observations at EDC (yellow) and DF (red). At both sites the ice-bedrock interface is at the pressure melting point (-2.2ºC). Right panel: model-data mismatch at EDC (yellow) and DF (red) for an ice flow-heat transport model forced by the optimized temperature histories (solid lines, ΔT_S of -5.5ºC at EDC and -3.2ºC at DF), and forced with water-isotope scaling of 0.7 ‰K^{-1} (dashed lines, ΔT_S of -9.0ºC at EDC and -7.5ºC at DF).

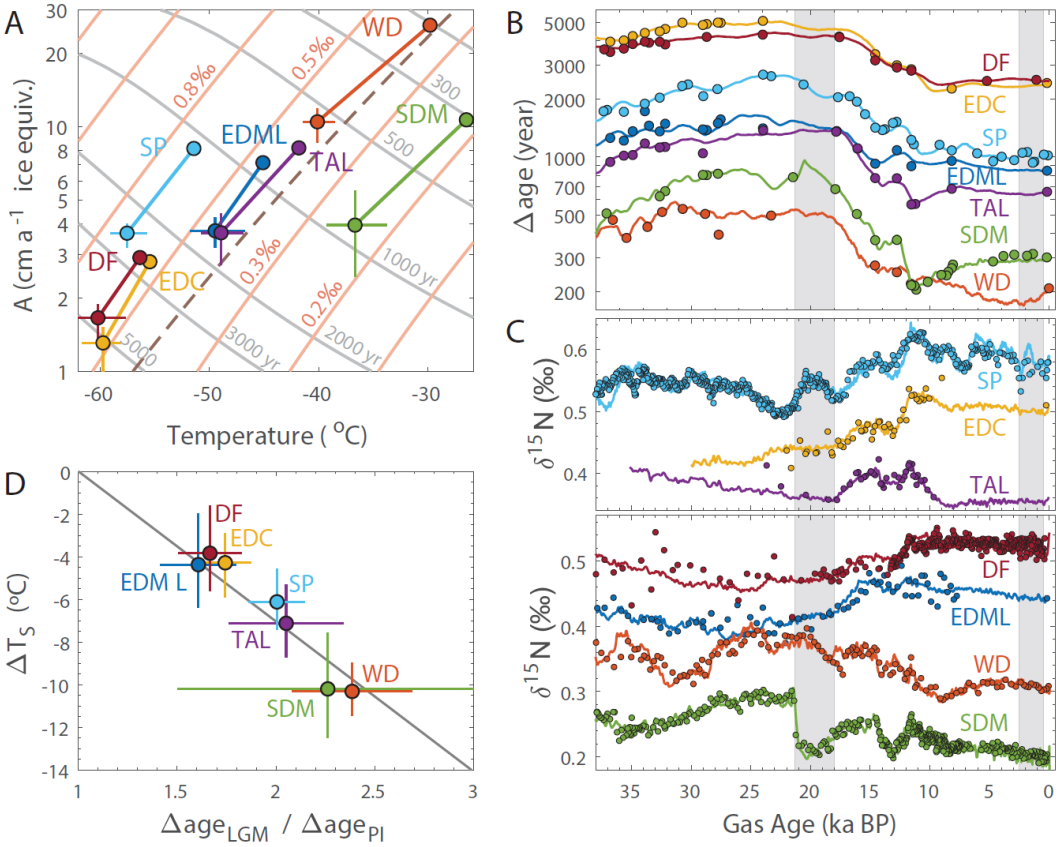

Figure 3. Δage-based temperature reconstructions. (**A**) Δage and δ^{15}N-isopleths (grey and salmon, respectively) in the steady-state Herron-Langway firn densification model as a function of T_S and A. Dashed line shows accumulation scaling via the saturation vapor pressure at the site (ignoring the atmospheric inversion). Reconstructed preindustrial and LGM conditions at the seven sites are indicated. (**B**) Model fit to empirical Δage constraints. Grey vertical bars denote the LGM (21.4-18 ka BP) and preindustrial (2.5-0.5 ka BP) periods. (**C**) Model fit to δ^{15}N data, divided over two panels to prevent overlapping curves. Data shown on the WD2014 timescale (*30, 31*). (**D**) Reconstructed ΔT_S versus ratio of LGM Δage over preindustrial Δage (with linear fit), showing the utility of Δage as a climate proxy.

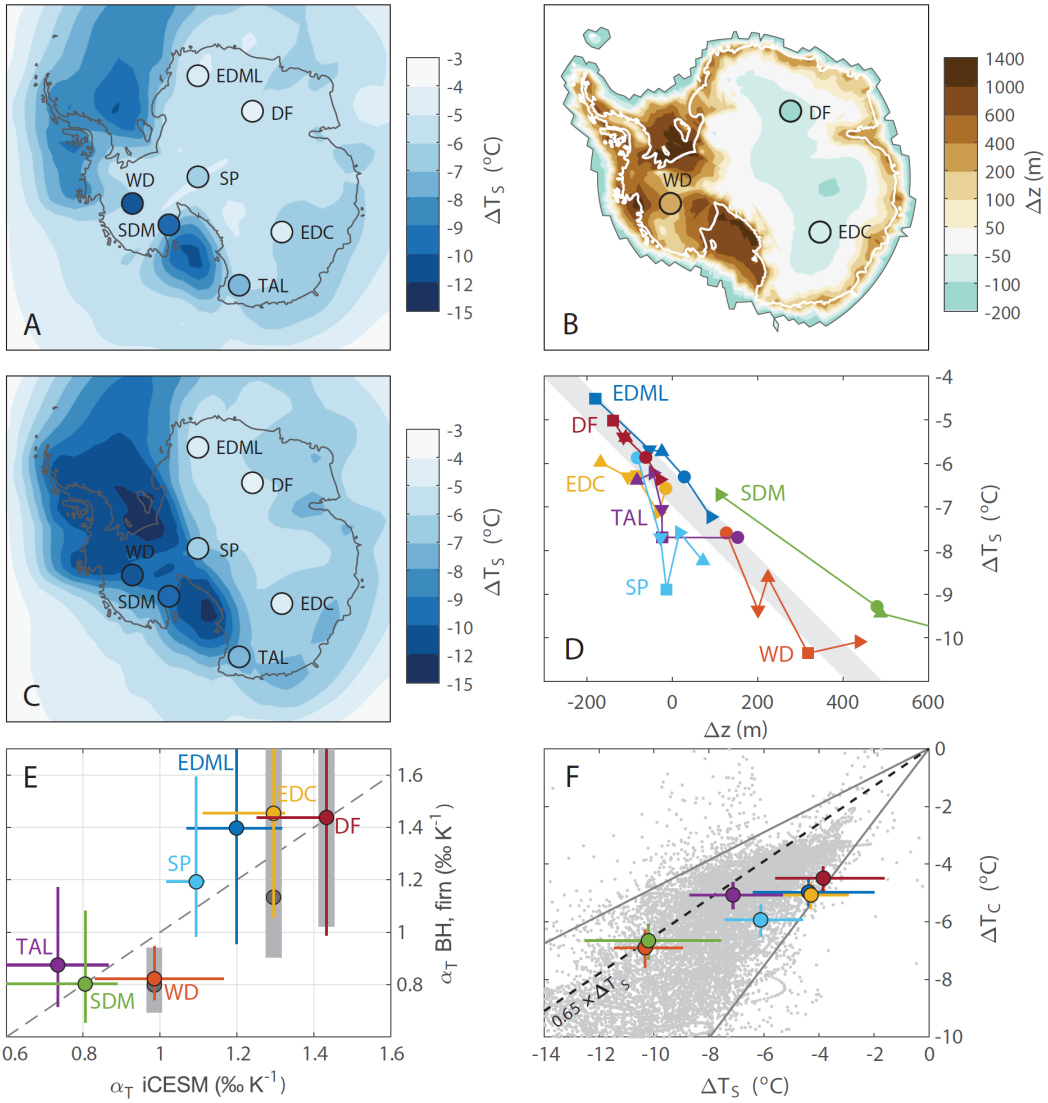

329

330 **Figure 4. Climate models and Antarctic topography. (A)** AOGCM simulations of ΔTs using
331 preindustrial ice topography in Antarctica (average of MIROC and HadCM models), with Δage-
332 based ΔTs reconstructions for the seven sites. **(B)** simulated LGM elevation anomaly (shaded,
333 average of five topographies) with LGM elevation anomaly of +310 m, -80 m, and -140 m at WD,
334 EDC and DF (*10*) **(C)** As in panel (A), but using LGM ice topography in Antarctica (average of
335 five LGM topographies and both MIROC and HadCM models). **(D)** Elevation change vs. ΔTs in
336 the AOGCM simulations (average of MIROC and HadCM models); symbols denote the different

LGM topographic reconstructions (see Fig. 1 caption for legend). The grey bar shows the dry adiabatic lapse rate. **(E)** Temporal isotope slope α_T from the iCESM model against our reconstructions (borehole in grey, Δage-based in colors). **(F)** ΔT_S vs ΔT_C from Δage-based ΔT_S and isotope-based ΔT_C (large dots with error bars) and from LGM-preindustrial AOGCM simulations (small grey dots, grey lines enclose the central 95% of estimates); black dashed line gives modern spatial slope (*2*). Models plotted are PMIP3 (except CNRM-CM5 that simulates $\Delta T_S > 0$ºC), PMIP4 (all model output publicly available), and all iCESM, MIROC and HadCM3 simulations used in this work; we show interior Antarctica (surface pressure > 800 hPa); T_C is taken to be the annual mean troposphere temperature maximum (typically around 500hPa). The models have an average preindustrial spatial dT_C/dT_S of 0.68 (range: 0.31 to 0.89) in interior Antarctica.

Content of the Supplementary Materials:

Materials and Methods

Figures S1 to S12

Tables S1 to S7

References 32-154 are only called out in the supplementary materials.

Science
AAAS

Supplementary Materials for

Antarctic surface temperature and elevation during the Last Glacial Maximum

Christo Buizert*, T.J. Fudge, William H. G. Roberts, Eric J. Steig, Sam Sherriff-Tadano, Catherine Ritz, Eric Lefebvre, Jon Edwards, Kenji Kawamura, Ikumi Oyabu, Hideaki Motoyama, Emma C. Kahle, Tyler R. Jones, Ayako Abe-Ouchi, Takashi Obase, Carlos Martin, Hugh Corr, Jeffrey P. Severinghaus, Ross Beaudette, Jenna Epifanio, Edward J. Brook, Kaden Martin, Jérôme Chappellaz, Shuji Aoki, Takakiyo Nakazawa, Todd A. Sowers, Richard Alley, Jinho Ahn, Michael Sigl, Mirko Severi, Nelia W. Dunbar, Anders Svensson, John Fegyveresi, Chengfei He, Zhengyu Liu, Jiang Zhu, Bette Otto-Bliesner, Vladimir Y. Lipenkov, Masa Kageyama, and Jakob Schwander

*Correspondence to: christo.buizert@oregonstate.edu

This PDF file includes:

Materials and Methods
Figures S1 to S12
Tables S1 to S7
Additional References 32-154

Other Supplementary Material for this manuscript includes the following:

Data Excel file S1

Materials and Methods

S1 Borehole temperature reconstructions at Dome C and Dome F

S1.1 Models and data

S1.1.1 Forward ice flow-heat transport model

We use a transient one-dimensional ice-flow model to compute the vertical-velocity profile through time:

$$w(\hat{z}) = -\left(\dot{b} - \dot{m} - \dot{H}\right)\psi(\hat{z}) - \dot{m} - \left(\frac{\rho_{ice}}{\rho_{firn}} - 1\right)\dot{b} \quad \text{(S1)}$$

where $\hat{z}$ is the non-dimensional height above the bed, $\dot{b}$ is the accumulation rate, $\dot{m}$ is the melt rate, $\dot{H}$ is the rate of ice-thickness change, ρ_i is the density of ice, ρ_{firn} is the density profile and $\psi(\hat{z})$is the vertical velocity shape function computed as:

$$\psi(\hat{z}) = \left(1 - \frac{p+2}{p+1}(1-\hat{z}) + \frac{1}{p+1}(1-\hat{z})^{p+2}\right) \quad \text{(S2)}$$

following Lliboutry (1979) where p is vertical velocity shape parameter (*32*). Firn compaction is incorporated through the right hand term in equation S1 and assumes a density profile that does not vary with time.

The heat equation following Cuffey and Paterson (2010) is (*33*):

$$\rho c_p \frac{\partial T}{\partial t} = \frac{\partial}{\partial z}\left(k\frac{\partial T}{\partial z}\right) - \rho c_p w \frac{\partial T}{\partial z} + Q \quad \text{(S3)}$$

where c_p is the heat capacity, T is temperature, k is the thermal conductivity, and Q is the heat production term, and z is the height above the bed. The firn density profile is modeled using the Herron and Langway model (*18*) matched to modern measurements to assure a smooth vertical velocity profile. Values of c_p are temperature dependent and calculated at each time step using the relationships from ref. (*34*). For k, we use three different relationships as described below (Section S1.2.1). The thermal conductivity in the firn is found using the relationship in ref. (*35*).

S1.1.2 Borehole temperature measurements

The EDC borehole temperature measurements were made in 2008 to a depth of 3235 m where the probe could no longer descend, possibly due to partial borehole closure. The temperature was extended to the pressure melting temperature of -2.18°C at the ice-rock interface at 3275 m. The principle of the probe is a four-wires circuit to measure the resistance of the temperature sensor (*36*). The upper 100 m of measurements are less reliable because they were made in the cased portion of the firn and have been excluded from our analysis. The data have been smoothed with a 5 m Hanning window. The uncertainty of the temperature measurements is 1 cK. The temperature profile is shown in Fig. 1 of the main text.

The Dome Fuji borehole temperature measurements were made in January 2013 on the DF-2 borehole using a Pt-100 resistance thermometer. As at EDC, the upper 100 m of measurements are less reliable because they were made in the cased portion of the firn and have been excluded from our analysis. The data are averaged over 50 m intervals to improve the signal-to-noise ratio. The uncertainty of the temperature measurements is 5 cK. The temperature profile is shown in Fig. 2 of the main text.

S1.1.3 Vertical velocity measurement

Phase sensitive radar measurements (ApRES) allow the determination of englacial vertical velocities (*37*). Three sets of measurements have been made with one year repeat intervals at Dome C. We focus on the highest quality measurements made in 2016 and 2017 (Figure S1). We use the ApRES measurements to constrain the Lliboutry *p* parameter by finding the best fit where the surface vertical velocity is also a free parameter (*38*). We do not fit the upper 200 m of measurements because these are affected by firn compaction which introduces additional uncertainty.

The uncertainty in the difference in vertical position of the ApRES antennas is larger than the changes in vertical position of the reflectors, such that a choice about the vertical velocity at the basal interface must be made. If the bed is frozen, then the basal vertical velocity can be assumed to be zero such that the ApRES measurements can be uniformly shifted (*38*). However, Dome C is potentially melting at the bed (*39*), so the basal velocity may not necessarily be zero. The deepest 15 m of ApRES measurements show near zero values, but from 15 to 30 m above the bed, the average is -0.0035 m a^{-1}, with an average of all 30 m of -0.0022 m a^{-1}. Therefore, there are a number of different ways to fit the vertical velocity, by either shifting the ApRES measurements, assuming a basal melt rate in the Lliboutry model fit, or both. Note that because of the way a basal melt rate affects the vertical velocity profile, shifting the ApRES measurements by a given value does not yield the same fit as imposing the same value as the modeled basal melt rate. We use 5 combinations of assumptions to find the range of potential of *p* values which are described in table S1. This give a range of values from p = 1.2 to 3.2 with the surface vertical velocities ranging from 0.03 to 0.033 m a^{-1}. The range of *p* values is similar to the range found from inverse modeling of the depth-age relationship (*39*). We use a value of p = 2 as our base scenario and p =1 and 3.5 to define the range of uncertainty. The surface velocities found in the fits are a few mm a^{-1} greater than the modern accumulation rate. This could indicate a small component of vertical thinning (a meter to a few meters per 1000 years) or the uncertainty associated with the ApRES measurements.

No ApRES data are available for the Dome Fuji site.

S1.1.4 Ice-flow model forcing: accumulation rate

The accumulation rate history is found using the best-fit vertical velocity profile to compute the thinning function and the timescale for EDC. We use a hybrid timescale where the most recent 57 ka use the timescale synchronized to WAIS Divide (*40*); prior ages are from AICC2012 (*41, 42*).

For Dome Fuji we use a similar approach in which the accumulation history is found using the thinning function in combination with the timescale of ref. (*43*).

S1.1.5 Ice-flow model forcing: surface temperature

The surface temperature history is found from the modern temperature by scaling the temperature change to the deuterium record (*3, 43*). The δD record is first interpolated to even spacing and smoothed with a 1000-year 7th order low pass filter. The surface temperature history, T_s, is found by

$$T_s = T_0 + \Delta T_s \tag{S4}$$

Where T_0 is the modern temperature and the change in surface temperature, ΔT_s, is found using equation S5 following ref. (*14*):

$$\Delta T_s(\delta) = {\alpha_T}^{-1} \int_t \dot{\delta}(t) dt \tag{S5}$$

where $\dot{\delta}$ is the time derivative of the filtered temporal δD record, t is time, and α_T the isotope sensitivity (temporal slope). In all model results presented here, α_T is a constant and is not allowed to vary through time.

S1.1.6 Inverse procedure

We use a gradient descent inverse method by defining the mismatch index:

$$J = \int_0^H \frac{[T(z)-\Theta(z)]^2}{\sigma^2_{\Theta(z)}} dz \quad \text{(S6)}$$

where $T(z)$ are the modeled borehole temperatures, $\Theta(z)$ are the measured borehole temperatures, and $\sigma_{\Theta(z)}$ are the uncertainties in the measured borehole temperatures. The temperatures in the firn are excluded (S1.1.2). The inverse procedure finds the values of $T_{surface}$, T_{bed}, and α_T, which all have a single optimum value (i.e. unimodal distribution).

S1.2 Results of temperature optimizations and uncertainty at Dome C

We first discuss the borehole temperature reconstruction at Dome C, where we have the better data constraints; we apply the lessons from Dome C to the Dome F reconstruction in Section S1.3.

We performed a series of optimizations for different prescribed ice properties and ice-flow parameters to evaluate the most likely temperature change and its uncertainty. As described below, we consider two types of uncertainty: (1) the temperature dependence of thermal conductivity (Section S1.2.1); and (2) parameter and forcing history (Section S1.2.2). Our best estimate of the LGM (18-21.4 ka BP) minus PI (0.5-2.5 ka BP) temperature change is ΔT_S = -5.5°C based on the average of three relationships for the thermal conductivity and our preferred forcings:

- a vertical velocity profile with p=2, based on ApRES vertical velocities (Section S1.1.3)
- 0.0005 m a^{-1} basal melting based on ref. (*39*)
- 100 m of deglacial thickening between 17 and 7 ka (Section S3.3)

The total uncertainty range is approximately ±1.9°C, which is the sum of the thermal conductivity uncertainty (Section 1.2.1, Table S2) and parameter/history uncertainty (Section S1.2.2, S1.2.3, Table S3 and Table S4).

S1.2.1 Thermal conductivity

The temperature dependence of the thermal conductivity (k) of ice is an important term for the inference of the LGM-Holocene temperature change at low accumulation sites. The standard relationship in Cuffey and Paterson (2010, p. 400) is from the review of Yen (1981), ref. (*34*). To evaluate the uncertainty due to the thermal conductivity, we use the relationship from two data sets that were not used in the Yen (1981) compilation (*44, 45*): Ross et al. (1978) and Waite et al., (2006). The thermal conductivity relationships are plotted in Figure S2, with the full temperature range in the left panel and only the temperature range of Dome C ice experiences in the right panel. Ross et al. (1978) reported only the fit, so the underlying data cannot be plotted.

The inferred temperature change and misfit are given in Table S2 and shown in Figure S3. The choice of relationship results in a 1°C difference in the inferred temperature change. Much of the model-data temperature misfit occurs in the bottom 500m. The near-bed temperature gradient, where the temperature gradient is nearly constant with depth, is not easily modeled. We test the impact of better fitting the near-bed temperature by decreasing the temperature dependence of the thermal conductivity. We also performed

tests in which we add strain heat in the basal ice to better match the basal temperature; because these last tests have the same impact as the changes in thermal conductivity on the inferred ΔT_S, we do not discuss these model runs further.

To assess the influence of the thermal conductivity of the deepest ice, we perform tests in which we adjust k for all ice with a temperature above -13°C. This temperature was chosen because it corresponds to the depth at which the ice grain size and fabric shows a distinct change (*46*), which is thought to be associated with the onset of migration recrystallization. The model-data fit is improved (Table S2) when we increase k linearly by up to 5% for the basal ice (-2.18°C). It is not clear how the changes in grain properties might impact k. Yen (1981) notes that k may be 5% greater along the c-axis of single crystals, which would be in the opposite direction to what we have applied because the c-axis fabric is becoming less vertically oriented near the bed (*46*); however, a study from the food science community suggests that the larger grain sizes (associated with slower freezing rates in that study) can cause a decrease k of 10%, although they do not report the grain sizes (*47*). While it is not clear how the change in grain properties should affect k, our adjustment provides a useful way to assess its impact on the inferred ΔT_S. The closer match to the basal temperature gradient allows the temperature misfit to be reduced. For each of the three published thermal conductivity relationships, applying the 5% k adjustment changes ΔT_S by around 0.25°C.

The temperature measurement uncertainty is 0.01°C at EDC. Therefore, we consider RMS values within 0.02°C of each other as equally viable solutions, and thus cannot reject any of the thermal conductivity relationships. We take the average of the six scenarios to define our best estimate of the magnitude of the LGM-Holocene temperature change. We conservatively use the full range of the six scenarios (1.2°C) as our uncertainty estimate.

S1.2.2 Uncertainty from parameter choices

We performed additional optimizations to assess the influence of the vertical velocity profile; the results are given in Table S4 and Figure S4. The range of possible p values for the vertical velocity profile from the ApRES measurements (S1.1.3) is very similar to published estimates (*39*). We use $p = 1$ and 3.5 as the lower and upper bounds and a preferred p value of 2. A smaller p value, which produces a vertical velocity profile more like that beneath a stable divide where a Raymond Arch develops (*48*), yields a larger LGM-Holocene temperature change, while a larger p value (more flank-like flow) yields a smaller temperature change. The change in ΔT_S upon varying p values within the specified range is around 0.68 °C (Table S4). Note that surface accumulation rates are coupled to the vertical velocity profile via the thinning function. When we alter the velocity profile, we alter the surface accumulation rates along with it to ensure internal consistency. Therefore, the uncertainty in past accumulation rates is also included in our error estimates (see Fig. S9 for the range of LGM accumulation rates in the borehole study).

The impact of basal melting was evaluated by assuming no basal melt or 1 mm/yr of basal melt instead of 0.5 mm a^{-1} based on Parrenin et al. (2007). No basal melt increases the magnitude of the LGM-Holocene temperature change compared to the base scenario, while increasing the basal melt does the reverse. The change in ΔT_S upon varying melt rates within the specified range is around 0.37 °C (Table S4).

We base our choice of thickness change on published simulated thickness histories (*49, 50*). The impact of deglacial ice sheet thickness changes was tested with alternative scenarios of either no thickness change, or doubling the amount of thickening between 17 and 7 ka to 200m, roughly spanning the range of responses seen in ice sheet model simulations (Section S3.3). Imposing no thickness change yields a 0.1°C larger ΔT_S. Given the low sensitivity to the prescribed elevation, we did not evaluate specific inferences from individual ice sheet models.

S.1.2.3 Temporal Variations in the shape of the vertical velocity

The shape of the vertical velocity profile is not necessarily fixed in time. A potential influence on the shape of the vertical velocity profile are changes in the temperature profile in the ice sheet; however, the low accumulation rates lead to heat transfer being dominated by conduction and thus only minor temperature variations deep in the ice sheet. Another potential influence is the development of a preferred crystal orientation fabric; however, the ice fabric at interior East Antarctic sites evolves slowly because of the low deformation rates (*46*) such that the evolution of the ice fabric is unlikely affect the vertical velocity pattern during the glacial termination.

Instead, the most likely reason for the shape of the vertical velocity profile to change is the position of the ice divide. As shown by the ApRES measurements and noted elsewhere (*39*), the shape of the vertical velocity profile has more of a quadratic character, consistent with the influence of lower deviatoric stresses near an ice divide (*48*), than the more linear shape predicted by Lliboutry (Eq. S2). This difference in shape of the vertical velocity profile beneath divides is what gives rise to so-called Raymond Arches commonly observed within coastal ice rises (*51*). No Raymond Arch is observed at EDC, likely due to the long characteristic time (100 ka) for which the divide position would need to be stable. The core and the ApRES measurements are near the ice divide today, such that any movement of the divide in the past would result in the more linear (larger p value) shape typical for sites away from a divide.

We evaluate the impact of a temporal variation in the vertical velocity shape function with a range of scenarios where we vary the onset time of the current vertical velocity profile (p = 2 for these scenarios) and the shape of the previous vertical velocity profile. We allow the transition in vertical velocity shapes to occur in 1 ka, at three different ages in the Holocene: beginning at 10 ka, 6 ka, and 2 ka. The previous shape of the vertical velocity profile is not known, other than it should be more linear (more typical of a flank site). We use p = 4, based on the vertical velocity profiles outside of the region of divide influence at Roosevelt Island (*38*); p = 7 based on recent measurements from Hercules Dome, another interior Antarctic dome site; and p = 15 which approximates a shape profile with deformation concentrated in the warm ice near the bed. The inferred ΔT_S for the nine scenarios is shown in Table S3; these scenarios use the Yen (1981) thermal conductivities and the standard forcing choices (S1.2); using the Waite et al., (2006) or Ross et al., (1978) thermal conductivities gives the same change in the inferred ΔT_S to within hundredths of a degree (*34, 44, 45*).

The inferred reduction in ΔT_S magnitude ranges from 0.44°C to 2.02°C with a mean reduction of 1.07°C. Because the shape of the vertical velocity profile is always more linear (or flank-like) in the past, the inferred ΔT_S is always smaller in magnitude. As the change in ΔT_S increases, the misfit to the borehole also increases. Thus, it is not clear that a variable vertical velocity shape function yields a more robust solution. Because we have no constraints on the shape of the vertical velocity profile for older ages and the timing of a transition, it is difficult to produce a quantitative estimate of the potential impact. Therefore, we do not directly include a temporally variable vertical velocity profile scenario in our "best estimate" independent borehole ΔT_S estimate and uncertainty. However, the sensitivity test described in this section suggests an asymmetrical source of uncertainty in the EDC borehole reconstruction, which we represent via an estimated uncertainty range that is not centered around our best estimate of ΔT_S = -5.5°C (but rather around ΔT_S = -5.0°C, which is halfway between our best estimate and the mean of the tests described in this section). We do note that the influence of time-variable p can reconcile the borehole- and Δage-based ΔT_S reconstructions.

S1.2.4 Additional temperature variability in borehole reconstructions

As part of the borehole reconstruction, we performed a variety of optimizations with α_T allowed to vary for different time periods. For example, in optimizations with two α_T scalings (one for the Holocene and one for the remainder of the record which is dominated by the LGM-Holocene change), the Holocene scaling

was often very large (resulting in little temperature variability) while the glacial scaling remained similar to that found in the single-scaling scenarios. Since the Holocene temperature variations are likely small, they have diffused away in the borehole temperature profile and cannot be resolved. In addition, the near-surface temperatures were less reliable such that the upper 150m were not included in the optimization, which may also inhibit the ability to infer an independent Holocene scaling. This lack of high frequency temperature information is a primary challenge of using borehole temperatures from low accumulation sites compared to sites such as WAIS Divide (15). Only the broadest information of glacial temperature is preserved, and we cannot reconstruct high frequency variations in the temperature history (*25, 52*).

S1.3 Results of temperature optimizations and uncertainty at Dome Fuji

We have performed a similar analysis for Dome Fuji as for Dome C; however, there are no ApRES vertical velocity measurements at Dome Fuji, and temperature measurements have a five times higher uncertainty at 0.05K. In addition, the ages and ice flow near the bed are not easily modeled, adding uncertainty in the vertical strain pattern. In particular, Dome F has a reversal of the thinning function near the bed, which layers in the deepest few 100 m having experienced less cumulative thinning than layers above it. In addition, the DF core has inclined (up to 50^{o}) internal layers in the deepest few 100 m, implying inhomogeneous bottom melting in the vicinity (*53*).

Therefore, the confidence in the inference of LGM-Holocene temperature change is lower than at Dome C. Our primary goal with the Dome Fuji borehole temperature measurements is to determine if they are consistent with the smaller ΔT_S inferred with our firn-based reconstruction method.

We report two model runs that envelope a plausible range of the LGM-Holocene temperature change at Dome Fuji based on the information from Dome C and previous modeling of Dome Fuji (*39*). Many more runs were performed, but their ΔT_S falls within this envelope. Using parameters for a small ΔT_S – Yen (1981) conductivity and no increase in basal thermal conductivity, a vertical velocity with p=4 and 0.3 mm a^{-1} of basal melt – we obtain ΔT_S = -1.8°C. Using parameters for a large ΔT_S – Waite et al. (2006) thermal conductivity with a basal increase up to 5%, p=1, and no basal melt – we obtain ΔT_S = -5.4°C. We thus report this range of -1.8°C to -5.4°C as the ΔT_S that is consistent with the DF borehole data, without making an attempt to provide a central or best estimate within this range as we feel that the problem is insufficiently constrained to do so. The reader may be tempted to view the midpoint of the interval (ΔT_S = -3.6°C) as a best estimate of DF cooling, but we do not endorse this interpretation.

The inferred DF ΔT_S range overlaps well with the firn-based reconstruction (Figure 1). The borehole reconstruction suggests that ΔT_S at DF was likely smaller than ΔT_S at EDC, as also seen in the firn-based reconstruction and climate model simulations. Importantly, the DF borehole reconstruction is inconsistent with a large ΔT_S of around -7.5 to -8°C, as suggested by traditional interpretation of the DF water isotope data (*8, 43*).

S2 Firn-based temperature reconstructions

S2.1 Ice Core data

S2.1.1 $\delta^{15}N$- N_2 data

Ice core $\delta^{15}N$-N_2 data used in this study are all available from published work (*30, 54-56*), with the exception of new Dome Fuji data first published with this paper (supplementary data). We combine ice sample data and lock-in zone firn air data (where available). Site $\delta^{15}N$-N_2 data are shown in Fig. 3C of the main text. All $\delta^{15}N$ data use the modern atmosphere as the reference scale.

Unpublished Dome Fuji $\delta^{15}N$ data are generated in three measurement campaigns. The first campaign (at Tohoku University, before 2001 (*57*)) covers 38 points from 563.3 to 992.9 m (LGM and older) with an uncertainty of 0.02 per mil (1 sigma). The second campaign (at Scripps Institution of Oceanography, 2007, (*58*)) covers 3 points from 462.5 to 478.5 m (Antarctic Cold Reversal) with uncertainty of 0.005 per mil. The third campaign (at the National Institute of Polar Research, 2016 - 2018) covers 293 points from 113.0 to 558.0 m (Holocene and Termination I) with uncertainty of 0.006 per mil (manuscript for method in preparation). There are offsets between the different datasets, thus 0.020 per mil is added to the Tohoku dataset and 0.010 per mil is added to the SIO dataset to match them with the NIPR dataset where they are overlapped.

For the SDM site we furthermore use published $\delta^{40}Ar$ data to calculate $\delta^{15}N$-excess to constrain abrupt warming at the 22ka event (*59*). An anomalous short-duration interval around 15.3 ka BP where SDM $\delta^{15}N$ approaches zero, thought to reflect a short-lived ablation event or catastrophic firn-break up (*59*), is removed from the SDM $\delta^{15}N$ data set and not interpreted here.

S2.1.2 CH_4 data

Ice core atmospheric CH_4 mixing ratio data are used for ice core synchronization in the gas phase (Fig. S5). Site CH_4 data were previously published for all sites except DF (*16, 42, 60-62*).

Dome Fuji CH_4 concentrations are measured at Tohoku University and Laboratoire de Glaciologie et Géophysique de l'Environnement (LGGE, currently L'Institut des Géosciences de l'Environnement). The Tohoku University data are collected in the same campaign as the $\delta^{15}N$ data using the method of ref (*57*) with analytical uncertainty of ~6 ppb (1 standard deviation). For the LGGE data, the air is extracted from the ice samples of ~50 g using an established melt-refreeze method, and analyzed by a gas chromatograph using a standard gas (499 ppb) for calibration, and an analytical uncertainty of 10 ppb (1 standard deviation) (*60, 63*). Before the synchronization, the LGGE dataset is shifted by +18 ppb to account for systematic offset in calibration scale relative to the Tohoku University scale; note that we use CH_4 only to constrain the event timing, and therefore the absolute concentrations are not important.

The SDM data used here are a compilation of previously published data (*62, 64-68*) measured at Oregon State University and Seoul National University using the same methods described in refs. (*64-67*).

The full DF and SDM CH_4 records are provided in the data supplement.

S2.1.3 Water isotope data

Water isotopic $\delta^{18}O$ (rather than δD) data are used at all sites, reported on the Vienna standard mean ocean water (V-SMOW) reference scale. These data are publicly available (*3, 43, 64, 69-75*). The ice core $\delta^{18}O$ data are corrected for the mean ocean $\delta^{18}O$ using ref. (*76*). The high-frequency structure in the firn-based reconstructions (Fig. S8) comes from the $\delta^{18}O$ data, while our firn-based reconstruction method only constrains magnitude of the long-term temperature change.

S2.1.4 Siple Dome volcanic ties

Volcanic tie points between the Siple Dome and WAIS Divide ice cores are given in the supplementary data files. We identify a total of 18 such volcanic ties based on established techniques: nine ties are found via matching Electrical Conductivity Measurement (ECM) records of volcanic activity (*55, 77*), and nine ties via the geochemical identification of tephras (*78, 79*). The volcanic tie points are shown on Fig S5. The oldest of these volcanic tie points is from 32ka BP, and thus the LGM and deglaciation are covered. Beyond 32ka we identify several ice-ice ties based on $\delta^{18}O_{ice}$ to extend the WD2014 chronology further back – these tie points have no impact on the ΔT_S presented here.

S2.2 Empirical Δage reconstruction

For all sites other than WD, we estimate Δage empirically by combing ice-phase volcanic matching and

gas-phase atmospheric methane (CH_4) matching to WD (*16*). Site Δage estimates are shown in Fig. 3B of the main text. WD was chosen for this purpose because of the high resolution CH_4 record (*80*), and small Δage at the site (*30*). The matching procedure is shown in Fig. S5, where we show volcanic ties (dots) and the site CH_4 records plotted on top of the WD CH_4 record. Volcanic ties to WD are published for all sites except SDM (*40, 42, 81-83*); SDM ties are provided in the data supplement and described below.

Conspicuous CH_4 features – such as Dansgaard-Oeschger (DO) oscillations and the onset of the deglacial CH_4 rise – are matched between the cores, thereby assigning a WD2014 gas age to the core being matched; the WD2014 ice age at that same depth is found from the volcanically synchronized time scales (*40*), allowing the gas age-ice age difference to be calculated. The sources of Δage uncertainty are: (1) uncertainty in the WD2014 Δage; (2) uncertainty in the WD CH_4 tie point determination; (3) uncertainty in the matched core CH_4 tie point determination (for example due to the finite time resolution of the CH_4 record); (4) uncertainty in age scale interpolation between volcanic tie points; these 4 terms are added in quadrature to estimate the Δage uncertainty. Note that WD has the smallest Δage of all cores considered here. The stated 2σ WD Δage uncertainty is 120 years during the LGM; which is a 23% relative uncertainty. However, at EDC the maximum Δage during the LGM is around 5000 years, in which case the same 120-year uncertainty only represents a relative uncertainty of 2.4%.

Figure S6 compares our empirical Δage estimates (dots with errorbars) to the Δage in the AICC2012 ice core chronology (grey curves) for the cores where this is available (TAL, EDML and EDC), as well as the Δage simulated in this study using a firn densification model (colored curves). We find good agreement.

The approach outlined above provides WD2014-consistent Δage estimates for all cores except WD; to apply our firn-based approach to WD we have to generate independent empirical Δage estimates. To do so we use published bipolar volcanic markers for Holocene and glacial period (*42, 84*). We match the WD CH_4 record to the NGRIP $\delta^{18}O$ at the midpoint of abrupt DO transitions, assuming a 25-year lag of atmospheric CH_4 behind Greenland climate (*30, 85, 86*); this provides a GICC05 gas age for each matched event, which is combined with a GICC05 ice age at the same depth (found from the bipolar volcanic synchronization) to calculate empirical Δage WD estimates. The uncertainty in these Δage markers is calculated as above for the other cores. The most prominent CH_4 feature around DO-2 is actually associated with Heinrich event 2 rather than with DO-2 (*80*). A comparison of the WD CH_4 record to GISP2 CH_4 identifies the location of the DO-2 CH_4 feature that is concurrent with the DO-2 thermal $\delta^{15}N\text{-}N_2$ fractionation signal (Fig S7B); this allows us to establish an empirical WD Δage constraint around this time by matching the WD CH_4 feature to Greenland records on the GICC05 time scale. Figure S7A compares the WD2014 and GICC05 Δage reconstructions for WD; during the glacial the WD2014 Δage is around 70 years smaller on average (*84*).

The differences between the two Δage estimates for WD can be transferred to all the cores in this study, and thus we have two sets of empirical Δage estimates for each core: one consistent with the WD2014 chronology, and one with the GICC05 chronology. The influence of the choice of base chronology on ΔT_S is estimated in the Monte-Carlo procedure (see below). The CH_4 match points, and the empirical WD2014 and GICC05 Δage estimates (with uncertainty) derived from it, are provided in the data supplement.

For the SDM site we furthermore derive a Δage constraint from the abrupt 22ka warming anomaly, which is seen in both the ice phase ($\delta^{18}O_{ice}$) and gas phase ($\delta^{15}N\text{-}N_2$ and $\delta^{40}Ar$).

In the remainder we will refer to the empirical Δage constraints as "Δage data" for the sake of brevity.

S2.3 Firn densification modeling

The rate of firn densification is sensitive to the temperature and the overburden pressure – with the latter determined by the time-integrated snow accumulation rate since the deposition of a layer. The time-variably surface temperature $T_S(t)$ and accumulation rate $A(t)$ histories are the primary controls on firn densification

rates, and firn densification models can be used to simulate the evolution of the firn layer through time (*17, 20, 87-91*). The $\delta^{15}N\text{-}N_2$ and Δage become fixed at the lock-in depth, providing observational constraints on past densification rates (*15, 88, 92*). Critically, the $\delta^{15}N$- and Δage-isopleths run perpendicular to each other in T_S,A-space (Main text Fig. 3A), meaning that if $\delta^{15}N$- and Δage are both independently known, a unique temperature and accumulation solutions exist (*20*); however such solutions are obviously subject to any biases present in the firn densification physics used.

To simulate past Antarctic firn evolution, we use a dynamical firn densification – heat transport model described elsewhere in the literature (*17, 30, 93, 94*). For the firn densification physics we use the overburden-pressure formulation of the Herron-Langway firn model; given by Equation 4c in Ref. (*18*). The model can be run in an inverse mode, where an automated routine is used to find the $T_S(t)$ and $A(t)$ solutions that optimize the fit to the $\delta^{15}N$ and Δage data; this approach was previously applied to Greenland records (*17*).

The inverse model adjusts the $T_S(t)$ and $A(t)$ input to minimize the cost function:

$$S = \sqrt{\frac{1}{N_\delta}\sum_i \frac{(d_i - m_i)^2}{u_i^2}} + \sqrt{\frac{1}{N_\Delta}\sum_i \frac{(D_i - M_i)^2}{U_i^2}} \quad \text{(S7)}$$

where d_i (D_i) are the $\delta^{15}N$ (Δage) data, m_i (M_i) the interpolated modeled values at the same depth, u_i (U_i) the data uncertainty, and N_δ (N_Δ) the total number of data. The climate forcings used in the modeling procedure are described by:

$$T_S(t) = T_{\text{init}}(t) + f_T(t) \quad \text{(S8)}$$

$$A(t) = A_{\text{init}}(t) \times [1 + f_A(t)] \quad \text{(S9)}$$

where T_{init} and A_{init} are the initial temperature and accumulation estimates; f_T and f_A are functions to correct our initial estimate, which are being optimized in the inverse modeling procedure. T_{init} is based on linear scaling of the site $\delta^{18}O$ (corrected for mean-ocean $\delta^{18}O$), using the isotope sensitivity constant α_{init} listed in table S5. The α_{init} values are chosen to be intermediate between the spatial slope α_S, and the LGM-PI α_T values reconstructed here (main text, Fig. 1). The reconstructed ΔT_S is independent of the choice of α_{init} in the 0.4 to 2.8 ‰ K^{-1} range that we have tested; the values used were found iteratively in two steps after a first attempt using the spatial slope isotope sensitivity as α_{init}. The choice of α_{init} mainly dictates the magnitude of high-frequency (decadal to millennial) temperature variability in the final reconstruction. Where available, A_{init} is based on de-strained layer-counted annual layer thickness data; this is only the Holocene at SP, and the last 31ka at WD. Elsewhere, A_{init} is likewise based on linear scaling of the water isotope record. All six variables in Eqs. (S8) and (S9) are plotted in Fig. S8.

The functions f_T and f_A are each defined using a series of control points a_i (white dots in Fig. S8), such that $f(t_i) = a_i$. At times in between the control points, the value of f is found via linear interpolation between the two adjacent control points. Because modern-day climatic conditions at the sites are known, we furthermore let $f(t=0) = 0$. Because our interest is in reconstructing ΔT_S, we decided to keep f_T (and in many cases f_A) constant through the duration of the LGM. This is implemented by requiring two adjacent control points to have the same value ($a_{i+1} = a_i$). This is indicated by thick grey horizontal bar connecting the two control points in Fig. S8. The values for a_i that minimize the cost function Eq. (S8) are found in an automated gradient method (*17*).

The timing of the control points was chosen to coincide with climatic change points in the $\delta^{18}O_{ice}$ records; for the deglaciation these are the onset of Heinrich Stadial (17.8 ka), the onset and termination of the Antarctic Cold Reversal (14.7ka and 12.8 ka), and the Holocene onset (11.6 ka). In other cases large features in the $\delta^{15}N$ record were used to select control points. Note that the number and timing of the control points

is different for each of the cores, as they were adjusted based on the unique characteristics and data availability at each of the cores. In general, cores with more data ($\delta^{15}N$ and Δage) have a greater number of control points.

As a first example of why certain control points were selected, we examine EDC and TAL where no $\delta^{15}N$ data are available older than ~23 ka BP. This means the $T_S(t)$ and $A(t)$ solutions are no longer uniquely constrained at those ages, and therefore we require f_T to have a constant value for all t older than 18ka BP (grey horizontal bars in Fig S8a and S8e). The model fits the EDC and TAL Δage observations prior to the LGM through making adjustments to f_A instead (keeping f_T constant).

As a second example, consider the SDM core, which has a large upward shift in $\delta^{18}O$ around 21.4 ka BP possibly driven by ice dynamics (*59*). We use control points on either side of the shift in both f_T and f_A to allow the model to adjust both the temperature and accumulation change across this transition. The transition is characterized by a large drop in $\delta^{15}N$ (the single largest feature in all $\delta^{15}N$ considered here), and both warming and a reduction in accumulation rate are needed to fit this feature (Fig. S8g).

As a third example, consider the SP core. Due to its flank-flow configuration the accumulation rate is much more variable than it would be at a dome, as the deposition site moves across spatial gradients in surface accumulation (*55, 95*). For this reason, SP requires more accumulation control points than the other cores do in order to fit the SP $\delta^{15}N$ data (Fig. S8d).

For the purpose of estimating ΔT_S the control points used during the deglaciation are most important. For all sites we conducted sensitivity studies in which the number of control points during the deglaciation is varied, and the changes in reconstructed ΔT_S are well within the spread estimated from the Monte Carlo uncertainty approach (Section S2.4). Therefore, we do not report on these experiments separately.

Besides the $T_S(t)$ and $A(t)$ histories, the densification model requires other site-specific, user-defined parameters (Table S5). The convective zone (CZ) thickness is estimated from firn air sampling data at all sites except TAL where such data is not available and we use a generic value of 5m. The surface snow density ρ_0 is estimated from density data at the sites. Following established methods (*96*), the lock-in density is estimated by $\rho_{LI} = \rho_{CO} - \rho_{diff}$, with the temperature-dependent close-off density ρ_{CO} given by the Martinerie equation (*97*), and ρ_{diff} a site-dependent lock-in zone thickness. We estimate ρ_{diff} from firn density and firn air sampling data, and fine-tune the value to best fit modern-day Δage and $\delta^{15}N$ at the site. It is established that lock-in zone thickness is proportional to site accumulation (*98*), and indeed we find low ρ_{diff} values at the low-accumulation EDC and DF sites (4 kg m^{-3} and 3 kg m^{-3}, respectively) and higher values at the high-accumulation WD site (10 kg m^{-3}). The recommended value for Greenland Summit is 14 kg m^{-3} (*96*). Intermediate-accumulation site SP has a thick lock-in zone, and we find an optimal ρ_{diff} of 15 kg m^{-3}. The ice sheet thickness H is taken as reported in the literature, and the site geothermal heat flux (GHF) is estimated by fitting the borehole temperature profile – note that the GHF estimation given in Table S5 is not optimized in any way, and therefore we recommend against interpreting these numbers. The GHF estimates in table S5 are lower bounds to the true GHF, because the effect of ice melting at the bed is not taken into account.

It has been hypothesized that dust (or perhaps calcium or fluorine/chlorine) may soften the ice, enhancing densification rates (*99-102*). The effect is not included here, see section S2.5 for a justification.

The optimal solutions presented in the main manuscript are derived using the dynamical description of the Herron-Langway (HL) densification model (*18*). However, other physical equations of firn densification are available, and we want to assess how the choice of model influences the result (Fig. S9). We compare the range of our dynamical HL Monte Carlo simulation (histogram, see also section S2.3 below) to results from running the Arnaud (*88, 103*), Barnola (*20, 87*) and Bréant (*89*) firn densification models in the inverse mode; we focus on the WD, EDC and DF sites that have borehole thermometry estimates (dots with error

bars). For all models we use the exact same experimental design: the same present-day T_S and A; the same T_{init} and A_{init}; the same Δage and $\delta^{15}N$ data; and the same T_S and A control points. We adjusted the ρ_{diff} model parameter for each model to obtain a good fit to the present-day Δage and $\delta^{15}N$ data, with the values given in Table S6. The model-specific ρ_{diff} adjustments are similar at all sites, suggesting they reflect model biases that are stable across a range of climatic conditions.

At WD, all models surveyed find a ΔT_S at WD in the -9.8 to -10.6ºC range, consistent with the borehole reconstruction. At EDC the HL and Bréant models find a ΔT_S that agrees with the borehole within uncertainty; the Arnaud and Barnola models reconstruct a somewhat small ΔT_S. At DF all models are in agreement within the borehole uncertainty range; yet again the Barnola and Arnaud models find smaller ΔT_S. We find at both cold sites that the HL and Bréant models reconstructs a larger ΔT_S than the Arnaud and Barnola models do, which is consistent with the fact that the former models have a lower effective activation energy than the latter models (Fig. S9, right panel), meaning that it requires a larger temperature change to induce the same change in densification rates. The Bréant model has a temperature-dependent effective activation energy (implemented as the sum of three Arrhenius terms) and is a modification of the Arnaud model (*89*); note that the Bréant model provides a much better fit to the borehole estimates than the Arnaud model does suggesting it is indeed an improvement over the Arnaud model.

Past accumulation is well constrained in our method – better in fact than the temperature is (compare the T_S and A envelopes in Fig. S8). The reason is an elemental physical one. The ice-equivalent lock-in depth (LIDIE), accumulation rate, and Δage are linked via the simple equation A = LIDIE / Δage. LIDIE is a scaled version of the lock-in depth (LID), and the scaling (of around 0.7) is very stable across a wide range of climatic conditions (*104*). Because in our method both Δage and the LID (from δ15N) are known, the accumulation rate is constrained very strongly. This is clearly visible in Fig. S9, where the four densification models find almost identical LGM accumulation rates. Uncertainty in $\delta^{15}N$, Δage, ρ_0, ρ_{diff} and CZ does impact the reconstructed A slightly, which is investigated in the Monte-Carlo study (S2.4). The A = LIDIE / Δage relationship is so fundamental that is independent of the firn densification model used to first order – the firn model choice only controls the scaling between LIDIE and LID, which have a ratio very close to 0.7 in all models and all climates (*104*).

This comparison suggests that the dynamical HL and Bréant models provide results in good agreement with the borehole temperature reconstructions over a large temperature range, and should therefore be given preference in simulating Antarctic firn dynamics at cold locations.

S2.4 Monte-Carlo uncertainty estimation

To estimate the uncertainty in our ΔT_S estimates we use a Monte-Carlo (MC) approach in which we randomly disturb the $\delta^{15}N$ and Δage data, and draw the user-defined model parameters randomly from a prescribed distribution (Table S5). For 1000 such iterations we perform the model inversion to estimate the $T_S(t)$ and $A(t)$, allowing us to describe the uncertainty in ΔT_S. Because inversion of the full dynamical HL model is computationally expensive, we instead use the steady-state version of the HL model for the MC uncertainty estimation. The procedure is identical to the dynamical model described above and uses Eqs. (S7) to (S9) to solve for $T_S(t)$ and $A(t)$. The steady-state model does not calculate the temperature profile, and we use a constant firn temperature gradient to account for thermal $\delta^{15}N$ fractionation by the GHF.

In each of the 1000 MC iterations we randomly draw each of the $\delta^{15}N$ data points from a normal distribution with a mean equal to the observation, and a standard deviation equal to the uncertainty in that observation. The Δage data points are each perturbed in two steps. In a first step we draw a random number c from a uniform distribution between 0 and 1; all the Δage data points D_i for that iteration are set to a weighted sum of the WD2014 and GICC'05-based Δage constraints (Fig. S7): $D_i = c \times D_i^{\mathrm{WD2014}} + (1 - c) \times D_i^{\mathrm{GICC'05}}$. In the second step, we add a random perturbation to each of the D_i that is drawn from a normal distribution

of zero mean and a standard deviation equal to the uncertainty (U_i). The ρ_0 and ρ_{diff} parameters are drawn from a normal distribution with a mean and standard deviation listed in Table S5. It has been suggested that the convective zone may be climate dependent, and possibly thicker during the LGM. The convective zone thickness is therefore described as the sum of two parts: 1) a climate-independent part that is randomly drawn from a normal distribution with a mean and standard deviation as listed in Table S5 (in case of a negative value, we re-draw until a non-negative value is obtained); 2) a climate-dependent part that is equal to a scaled version of the site $\delta^{18}O$ record (such that it equals zero in the PI and one in the LGM) multiplied by a random number drawn from a uniform distribution between 0 and 5 (the LGM CZ is thicker or equal to the PI CZ).

The bias of the steady-state approach is calculated by taking the difference between the $T_S(t)$ and $A(t)$ solutions found in the dynamical HL inversion and the steady-state HL inversion, where both use the preferred parameter settings; all steady-state HL solutions in the MC study were corrected for this bias. In Figure 1 of the main text we report the mean and 2σ standard deviation of the ΔT_S distribution found in the MC study – this differs from the dynamical HL solutions by 0.08ºC on average.

S2.5 The glacial $\delta^{15}N$ data-model mismatch in previous studies

For several of the East Antarctic sites (EDC, DF, SP, EDML; see Fig. 3 of the main text) the firn thickness during the glacial period as indicated by $\delta^{15}N$ is thinner than it is at present. However, densification models, when forced with a ΔT_S of around -9ºC, simulate a thicker glacial firn column (increased $\delta^{15}N$) than at present. This has led to the notion that there is a $\delta^{15}N$ data-model mismatch in the glacial period in East Antarctica (*56, 89, 105, 106*). Note however, that this behavior is not observed for the West Antarctic WD and SDM cores that have increased glacial $\delta^{15}N$, nor at the TAL site (based on the limited available $\delta^{15}N$ data). Moreover, densification models have been very successful at simulating Greenland firn evolution during the glacial time (*17, 20, 90, 91, 107*). Barring anomalous situations (such as surface melt and shear zones of ice streams), we are not aware of a single study in which firn models fail to simulate the basic properties of firn of interest here (meter-scale density, lock-in depth, Δage) within a reasonable error margin.

One hypothesis for the low glacial $\delta^{15}N$ is a thickened CZ during the LGM (*105, 106*). To explain the low glacial ^{15}N requires up to 40m of CZ thickness during the LGM at DF (*108*). Such deep convective mixing has not been observed in present-day Antarctica; the deepest documented CZ occurs at the extreme Antarctic Megadunes site, a zero-accumulation site where deep thermal cracks act as conduits for air mixing down to ~23 m depth (*108*). Glacial records of chemistry, water isotopes, volcanic deposition and atmospheric composition of the cores used in this study all provide evidence for continuous and hiatus-free ice accumulation through the glacial period, precluding the kind of conditions that drive deep mixing at Megadunes. Also, low-accumulation dome sites (like e.g. Dome C) today tend to have thin rather than thick convective zones. Overall there is limited support or evidence for this hypothesis (*105*).

Another proposed solution to the glacial ^{15}N mismatch is linked to the hypothetical influence of dust (or perhaps calcium or fluorine/chlorine) in softening the firn, thereby enhancing densification rates (*99-102*). In this hypothesis, the high dust loading of glacial ice enhances densification rates, thereby thinning the firn column as reflected in low glacial $\delta^{15}N$. At the WD site, where past $T_S(t)$ and $A(t)$ are well-constrained by borehole thermometry and annual-layer counting respectively, it was found that including the effect of dust softening only acted to deteriorate the fit to observational data (*30*). Recently, a multi-site study found that while including dust softening improved the model-data agreement at EDC and EDML, it worsened the agreement at WD and the Greenland NGRIP site (*89*). Generally, in Greenland cores, where dust loading is an order of magnitude larger than in Antarctica, densification models are successful in simulating firn evolution without taking the hypothesized softening effect of dust into account (*17, 20, 90, 91, 107*). If the hypothesized dust softening effect were true, it should work at all locations and time periods; since it does not, we believe this hypothesis can by eliminated.

LGM climate in interior East Antarctica has no modern analogues, and therefore falls outside the calibration range of densification models – perhaps casting doubt on their ability so simulate such climates (note that this cannot be a complete solution to the "glacial $\delta^{15}N$ problem", because EDML, SP and Law Dome all exhibit low glacial $\delta^{15}N$, yet remain within the densification model calibration range). Bréant et al. provide an interesting variation on this idea, by suggesting that firn densification models are too sensitive to temperature at cold conditions (*89*). They re-tune the Arnaud model to reduce its sensitivity at low temperatures, thereby improving the fit to glacial $\delta^{15}N$ data. There are two important caveats: (1) they invoke a hypothetical densification process with an activation energy of 1.5 kJ/mol – at least 10 times smaller than any known densification or vapor movement processes in firn; (2) the model (when forced with $\Delta T_S = \sim -9^oC$) still requires dust softening to satisfactorily fit $\delta^{15}N$ data at EDML and EDC (*89*), as well as at DF (Anaïs Orsi, personal communication 2019). In our analysis, the performance of the Bréant model at low temperatures is very comparable to the HL model (Fig. S9).

Our work suggests an alternative solution to the glacial $\delta^{15}N$ data-model mismatch: all previous firn modeling work has overestimated glacial cooling in East Antarctica. We find that the HL densification model can fit Δage and $\delta^{15}N$ data for all Antarctic core sites using $T_S(t)$ forcing consistent with the borehole temperature profiles, and $A(t)$ forcing consistent with de-strained layer thickness. The spatial ΔT_S pattern we find correlates well (r=0.90) with that in GCM simulations using realistic Antarctic LGM topography.

Our work uses the HL densification model, which is calibrated over a temperature range from -15°C to -57°C (*18*). The lowest LGM temperatures in our reconstructions are -60°C (Dome F), which is just outside the HL calibration range. However, for the two coldest sites (EDC and DF) our firn-based ΔT_S is in good agreement with the borehole temperature profile (main text Fig. 2), suggesting the model performs adequately under such cold climatic conditions. Moreover, ΔT_S at the cold DF site is very similar to ΔT_S at the nearby EDML site, where LGM temperatures of around -50°C are well within the HL calibration range.

S3 Climate model simulations

S3.1 HadCM3 model

We use the fully coupled ocean-atmosphere model HadCM3B M1 (*109, 110*). This model has a long history of use in paleoclimate simulations, more recently, has been found very useful for sensitivity testing past climates (*111-114*). Briefly, the atmosphere model has a horizontal resolution of 96×73 gridpoints (3.75°longitude×2.5°latitude) with 19 hybrid levels (sigma levels near the surface, changing smoothly to pressure levels near the top of the atmosphere). The ocean component has a horizontal resolution of 288×144 grid points (1.25°×1.25°) and in the vertical there are 20 depth levels.

The HadCM3 model simulations presented here are extended from a more than 5000 year long LGM simulation of the model using the PMIP2 protocol (*111, 115*). This is broadly similar to the PMIP3 (*116*) protocol (GHG, land sea mask, vegetation) but differs in the ice sheet reconstruction: PMIP2 uses ice5G, PMIP3 uses a composite (*116*). In our simulations, since we vary the Antarctic topography, the difference between the PMIP2 and PMIP3 lies only in the topography of the Northern Hemisphere ice sheets. HadCM3 has a climate sensitivity (global warming in response to doubling of CO_2) of around 3.5°C; the LGM simulation has an Atlantic Meridional Overturning Circulation (AMOC) strength of ~17.2 Sv.

All sensitivity simulations (section S3.3) are run for an additional 500 years (on top of the LGM spin-up) with the analysis performed on years 50-150. There are negligible differences between results for any 100 year period after an initial 50 year spin up.

LGM surface atmosphere cooling in HadCM3 is -5.4 °C in the global mean; -3.2°C in the tropics (30°S-30°N); -10.6°C in the northern hemisphere extratropics, and -5.0 °C in the southern hemisphere extratropics.

Northern hemisphere extratropical surface cooling is much greater than other zonal bands due to the large albedo and lapse-rate forcing of the large NH ice sheets (Laurentide and Fennoscandian).

S3.2 MIROC model

We further perform numerical experiments with the Model for Interdisciplinary Research on Climate 4m (MIROC4m) AOGCM (*117*). This model consists of an atmospheric general circulation model (AGCM) and an oceanic general circulation model (OGCM). The AGCM solves the primitive equations on a sphere using a spectral method. The horizontal resolution of the atmospheric model is ~2.8˚ and there are 20 layers in the vertical. The OGCM solves the primitive equation on a sphere, where the Boussinesq and hydrostatic approximations are adopted. The horizontal resolution is ~1.4˚ in longitude and 0.56˚ to 1.4˚ in latitude (latitudinal resolution is finer near the equator). There are 43 layers in the vertical. Note that the coefficient of horizontal diffusion of the isopycnal layer thickness in the OGCM is slightly increased to 700 m^2s^{-1} compared with the original model version (300 m^2s^{-1}) that was submitted to PMIP2. The current model version has been used extensively for modern climate, paleoclimate (*118*), and future climate studies (*119*). The climate sensitivity of this model is 4.3 ℃ (*119*); the model has an LGM AMOC strength of ~7 Sv, a shoaled mode of northern source deep water in the Atlantic and expanded southern source deep water, in good agreement with reconstructions based on North-Atlantic $\delta^{13}C$ and $\Delta^{14}C$ marine sediment data (*120*).

Ice sheet topography sensitivity experiments are initiated from a previous LGM experiment (*53, 120*), which is forced with PMIP3 boundary conditions (*116*). Based on this original experiment, the topography of the Antarctic ice sheet is modified following multiple reconstructions (Section S3.3); the extent of Antarctic ice sheet is unchanged from the original PMIP3 LGM experiment. These sensitivity experiments are integrated for 1000 years and the climatology of year 401-500 is used for analysis. The main result does not depend on the choice of the period used for the analysis.

LGM cooling in MIROC and HadCM3 is respectively -5.2 ºC in the global mean; -2.7ºC in the tropics (30ºS-30ºN); -12.7ºC in the northern hemisphere extratropics, and -3.1 ºC in the southern hemisphere extratropics. Northern hemisphere extratropical surface cooling is much greater than other zonal bands due to the large albedo and lapse-rate forcing of the large NH ice sheets (Laurentide and Fennoscandian).

S3.3 Ice sheet topography sensitivity experiments

We perform a series of sensitivity experiments with both models in which we vary the shape of the LGM ice sheet over Antarctica using a variety of reconstructions. For all of these LGM ice sheets we vary the topography but not the ice sheet extent (or ice mask), to ensure that we are only investigating the contribution of topography and not the albedo contribution to regional surface temperatures. For some reconstructions this results in a less extensive ice sheet in Antarctica, for others a more extensive ice sheet. In these latter cases the additional ice is set to 5m elevation. When adjusting the Antarctic ice sheet we follow the PMIP protocol of adding the LGM to preindustrial elevation anomaly to the models preindustrial topography. Since the PI topography in some reconstructions used is not the same as preindustrial topography in the climate model, this means that the absolute LGM topography in these cases differs between the climate model and the original reconstruction; the LGM-PI ice anomaly is the same as in the original publications, however.

To isolate the climatic and topographic contributions to LGM cooling, we furthermore run an LGM simulation in which we use full LGM boundary conditions (including LGM Antarctic ice mask), but PI topography in Antarctica. In this simulation we keep the ice sheet elevation constant relative to the modern geoid; since the LGM sea level was 120 m lower than during the PI, this means that in this simulation the ice sheet elevation is 120 higher relative to the contemporaneous sea level.

We perform LGM climate model simulations with 8 different ice sheet topographies; 7 from LGM ice sheet reconstructions (*29, 50, 116, 121-125*) and the last being the PI topography. All the LGM-PI ice elevation anomalies are shown in Fig. S10, expressed relative to the PI geoid rather than contemporaneous sea level

(hence the 120 m elevation drop over the Southern Ocean). Each of these topographies was used to force both the MIROC and HadCM3 climate models, with the simulated ΔT_S shown in the right two columns of Fig. S10. Unless noted otherwise, we only consider the first five of the LGM topographies shown in Fig. S10 in our analyses. The other two are only shown here for completeness and historical reasons; the Ice-5G reconstruction has been superseded by Ice-6G, and the PMIP3 ice sheet has highly unrealistic ice loading (up to 2500 m surface elevation gain) over interior West Antarctica.

For all topographies (main text Fig. 1, Fig. S10), the HadCM3 model on average simulates 2.2ºC more LGM cooling than MIROC does across Antarctica (except for SDM). The same difference is seen in the SH extratropical (90º-30ºS) zonal averages given earlier. The core site average ΔT_S is -6.3 ± 0.7 ºC in MIROC and -8.5 ± 1.1 ºC in HadCM3 (2σ spread between topographies); it is -6.6 ± 1.8ºC in our firn-based reconstructions (Fig. 1, main text). The MIROC model thus matches our reconstructions more closely on average – the only exception is the WD site. The PMIP4 multi-model ensemble has a core site average ΔT_S of -7.8 ± 4.6 ºC using the Ice-6G topography.

Next we address the ΔT_S spatial pattern, which is due to a combination of a lapse rate effect due to the elevated topography and a dynamical effect caused by changed atmospheric circulation again due to the elevated topography. The overall effect of ice sheet topography is comparable between the models, with both models showing a lapse-rate cooling with increased site elevation following a lapse rate of around -10ºC km^{-1}, close to the dry adiabatic lapse rate (main text, Fig. 4d).

Figure 1 of the main text compares the simulated ΔT_S from both models to the data-based reconstructions. In terms of the absolute changes, MIROC provides a better fit to the reconstructions than HadCM3 does, with the exception of the WD site where HadCM3 provides the closer fit. In terms of the spatial pattern both models perform equally well; we find a Pearson correlation of $r = 0.86$ between the firn-based ΔT_S and the HadCM3 simulation (average of 5 topographies), and for MIROC this is 0.88; when averaging both models, the correlation increases to 0.96. Of all the topographies considered, Pollard and DeConto (2009) and Whitehouse *et al*. (2013) give the best correlations (0.96 and 0.91, respectively). For the models in the PMIP4 LGM ensemble (section S3.6), we find correlations ranging from $r = 0.46$ to $r = 0.93$ (average single-model $r = 0.79$); interestingly, when averaging the models we again find an increase in correlation to $r = 0.95$, which is higher than for any of the individual models. It is clear that AOGCMs broadly match the spatial pattern seen in the firn-based reconstructions.

S3.4 Isotope-enabled CESM model simulations

The LGM and preindustrial simulations used the water isotope-enabled Community Earth System Model version 1.3 (iCESM1.3) with a horizontal resolution of 1.9 × 2.5° (latitude × longitude) for the atmosphere and land, and a nominal 1° for the sea ice and ocean. The physical climate model of iCESM1.3 is an upgraded version of CESM1 (*126*) with small changes in the atmosphere component. The water isotope capability of iCESM has been documented and validated against present-day and paleoclimate observations (*127*).

The iCESM1.3 LGM simulation was performed following the protocols from the Paleoclimate Modelling Intercomparison Project phase 4 (PMIP4) with the LGM (at 21ka) values of greenhouse gas concentrations, Earth orbital parameters, and the ICE-6G reconstruction of land ice sheets (*19, 125*). Ocean state in the simulation was initialized from an existing equilibrated LGM simulation that used an older version of CESM (*128*). The isotopic composition of seawater was initialized from the Goddard Institute for Space Studies observations with a constant value of 1.05‰ added to account for the glacial enrichment due to the increased LGM ice sheets. The iCESM1.3 LGM was integrated for an additional ~1,000 years. The TOA energy imbalance averaged over the last 100 years is approximately –0.1 W m^{-2}, indicating the surface climate has reached a quasi-equilibrium glacial state. Readers are referred to ref. (*129*) for details of the LGM and corresponding preindustrial simulations.

S3.5 Brief review of published isotope-enabled LGM simulations

LGM to present water isotope changes in Antarctica depend on many key factors including (but not limited to) southern hemisphere SST patterns (*6*), sea ice extent (*7*), ice sheet elevation (*8*), atmospheric transport pathways (*130, 131*), precipitation seasonality (*132*), stratosphere-troposphere vapor exchange (*133*) and post-depositional snow redistribution and snow-vapor isotope exchange (*9, 134*). Isotope-enabled general circulation models (iGCMs) seek to capture the aforementioned physical processes making them an invaluable tool in understanding isotopic variations in Antarctica. However, most if not all of the above-mentioned factors have large uncertainties associated with them, and some processes are not typically simulated in iGCMs (such as stratospheric exchange and post-depositional isotopic exchange). iGCMs typically capture the present-day spatial slope well (*2*), yet $\delta^{18}O$ offsets at individual sites of 10 ‰ or more (i.e. twice the LGM-PI $\delta^{18}O$ difference) are not uncommon.

Owing to both the complexity of the system and the large uncertainty in individual components, iGCMs simulate a wide range of values for the temporal slope α_T (here: the ratio of the LGM-PI change in $\delta^{18}O$ of precipitation over ΔT_S). Considering only studies that investigate the LGM-PI difference, iGCMs have suggested α_T values in central East Antarctica that are:

- in the 0.1 to 0.6 ‰ K^{-1} range, and thus considerably lower than the spatial slope (*6, 8, 11, 135*)
- in the 0.6 to 0.9 ‰ K^{-1} range and thus comparable to the spatial slope (*5, 6, 8, 12, 136*)
- in the 0.9 to 1.6 ‰ K^{-1} range and thus considerably larger than the spatial slope (*12, 137*) (this study)

Note that it is not trivial to compile the temporal slopes consistently, given that papers report values at different locations and time intervals, and the fact that the simulated temporal slopes tend to be highly variable between nearby location (*8, 138*). A systematic iGCM intercomparison would be highly valuable to the field. Studies that are listed more than once may report results from different models, models run under different boundary conditions, or have large differences between central East Antarctic core sites.

It is very challenging to assess how the full uncertainty in all the aforementioned processes influences the simulated α_T. However, the inter-model spread can serve as an uncertainty estimate of how well the various processes are constrained in the models. We remove the high and low extremes from the simulated α_T range, and estimate that central East Antarctic LGM-PI α_T as simulated by iGCMs is in the 0.3 to 1.4 ‰ K^{-1} range. For EDC and DF this implies a surface temperature ΔT_S of 4ºC to 21ºC, and 4ºC to 18ºC, respectively (rounded to nearest integer, and ice core $\delta^{18}O$ corrected for mean ocean $\delta^{18}O$).

S3.6 Paleoclimate Modeling Intercomparison Project Phase 4 (PMIP4)

Here we use the multi-model LGM ensemble from the PMIP4 project, which includes the following 10 models: AWI-ESM1, AWI-ESM2, CCSM4-UofT, CESM1.2, iLOVECLIM1.1.1 (GLAC-1D), iLOVECLIM1.1.1 (ICE-6G-C), INM-CM4-8, IPSL-CM5A2, MIROC-ES2L, and MPI-ESM1.2. All models use the Ice-6G LGM ice sheet topography (*125*) except for iLOVECLIM1.1.1 (GLAC-1D), which uses the GLAC-1D model (*29*). For a description of the PMIP4 LGM experiment, a description of the various models, and an assessment of their performance, we refer to previous work (*19, 139*).

S4 Elevation change from ice core Total Air Content data

S4.1 Data description and cut-bubble correction

We use total air content (TAC) data as a paleo-elevation proxy from the WD, EDC and DF sites. Data from EDC were previously published (*22*), for WD and DF we present previously unpublished data.

For the DF core we use two separate data sets. A first series of measurements were carried out at LGGE/IGE, Grenoble, France, using an original barometrical method implemented with an experimental setup called

718 STAN (*140*). The STAN allows precise evaluation of the pressure and temperature of air extracted from an
719 ice sample by its melting-refreezing under a vacuum in a volume-calibrated cell. After correcting the
720 measured pressure for the partial pressure of saturated water vapor and of the calibrated volume for the
721 volume occupied by refrozen bubble free ice, the TAC is calculated using the ideal gas law. The ice samples
722 used in STAN have a mass of about 25 g and a regular shape of a rectangular parallelepiped or cube, which
723 facilitates estimation of their specific surface. A second, independent dataset of DF TAC was generated at
724 Tohoku University (TU), Sendai, Japan, as part of the gas chromatography measurements (*57, 141*). Briefly,
725 an ice sample of ~300 g was melted in a vessel under vacuum, and the extracted air was transferred to a
726 sample tube after removing water vapor. The pressure of the sample air was measured at room temperature
727 in a combined volume consisting of the sample tube, gas chromatograph inlet and sample loops, with a
728 semiconductor pressure transducer. The volumes of the sample tubes and other parts were calibrated prior
729 to the ice core measurements, and the temperature and pressure of the laboratory were used for normalizing
730 the results. The latter data set was scaled linearly by 0.975 to bring it into agreement with the calibrated
731 STAN data set; the origin for the discrepancy is not clear, but we note that the two datasets agree excellently
732 in terms of relative variations

733 Both DF datasets were corrected for the "cut-bubble effect", which is the gas loss from air inclusions
734 (bubbles, gas hydrates and relaxation features such as air cavities) cut at the surface of the sample. The
735 correction depends on the specific surface of the ice sample and the size of air inclusions (*142*). The size of
736 air inclusions was measured under a binocular microscope in 2-4 mm thick sections of ice cut in parallel
737 with the samples used for STAN measurements; for the gas chromatography data set we used linear
738 interpolation to find the bubble diameter at the sample depths.

739 The absolute precision of the STAN TAC measurements has been estimated to be within ± 0.6%, and of the
740 gas chromatography TAC measurements better than 1%. However, the overall error of the obtained TAC
741 values amounts to 1% due to the uncertainties in the cut-bubble correction. The average reproducibility of
742 the STAN measurements performed in the same horizontal slice of an ice core has been confirmed to be
743 better than 1%.

744 WAIS Divide TAC and methane were measured concurrently at Oregon State University using a wet-
745 extraction process following ref. (*143*) with minor changes; the method is similar to those used elsewhere
746 (*97, 144*). The measurements presented were made over intervals between 2006 to 2017. The sample size
747 was 50 to 60 g, and the majority of samples were run in duplicate. The melt-refreeze process does not
748 extract all air, and a solubility correction is applied. The size of the correction is found by performing a
749 second melt-refreeze extraction on the frozen sample water, which allows estimating the magnitude of the
750 dissolved air fraction. The solubility correction as a percent of the initial pressure is determined to be 1.3 ±
751 0.2 % for Holocene samples and 1.3 ± 0.1% for the deeper samples. Replicate analyses suggest a
752 reproducibility of better than 0.5%. As for DF, we correct for the cut-bubble effect following ref. (*142*). We
753 assume uniformly distributed spherical bubbles using published bubble radius data (*145*). Beyond 562m
754 depth, radius values are extrapolated using a linear fit with the bubble correction estimated to be 0 at 1600m
755 due to the completion of the bubble-clathrate transition.

756 Panel S12d compares TAC signal differences between the LGM and PI, where we have subtracted the PI
757 mean TAC value from the records (thereby aligning them during the PI). We find that during the LGM,
758 TAC at EDC and DF was elevated relative to the TAC at WD; the difference is around 7 mL kg^{-1} for DF-
759 WD, and 6 mL kg^{-1} for EDC-WD.

760 **S4.2 Data corrections and Elevation change**

761 It is challenging to interpret TAC in terms of absolute elevation change; our approach instead aims to
762 reconstruct the difference in LGM elevation anomaly Δz between WAIS and EAIS (which we term $\Delta\Delta z$).
763 Quantitative interpretation of TAC is possible because: (1) we investigate relative changes in TAC between

WD and DF/EDC, which means that the large influence of insolation on both records cancels out to first order; and (2) we only investigate the LGM and PI time slices, both of which are equilibrium firn states not impacted by transient TAC anomalies due to changes in overburden pressure and/or changing firn temperature gradients (*146*).

To convert the TAC data into elevation change, we first need to apply several corrections. The first and most critical is the correction for insolation (*22*). Because we are interpreting relative TAC changes (WD vs. EDC/DF) rather than absolute ones, most of the insolation signal is canceled out because it affects TAC records at both locations. However, the elevation component of TAC is recorded on the gas age scale, while the insolation component of TAC is recorded on the ice age scale, and hence the cancellation effect is incomplete. To account for this, we apply an insolation correction based on the integrated summer insolation (Fig. S12c) as is the standard in the literature (*22, 146*). Eicher et al. (2016) report a sensitivity of -5.7 mL kg^{-1} GJ^{-1} at NGRIP (*146*), while the data from Raynaud suggest a sensitivity of -6.6 mL kg^{-1} GJ^{-1} at EDC. Here, we shall use the average of these two estimates as our optimal correction scenario. To assess the uncertainty in the correction, we furthermore construct a scenario with no insolation correction, and a scenario in which we use a correction that is twice as large as the optimal scenario.

A second correction is for the temperature at bubble close-off, which impacts TAC in two ways: (1) it changes the pore volume at close-off, which we calculate using ref (*97*); and (2) it impacts the number of moles trapped at a given volume and pressure via the ideal gas law. These two effects cancel each other out almost completely; the LGM TAC correction is 0.001, 0.0005, and 0.0004 mL kg^{-1} at WD, EDC and DF, respectively.

Third, TAC reflects the elevation of the close-off depth, and not the ice surface of interest. We apply a correction using the simulated close-off depth from the firn model, which is well-constrained by $\delta^{15}N$ data. The LGM close-off depth anomaly relative to the PI was +7 m, -12 m, and -8 m at WD, EDC and DF, respectively. We do not assess the uncertainty in the close-off depth correction given that it is negligible compared to the uncertainty in the insolation correction.

The TAC changes are then converted to relative elevation change ($\Delta\Delta z$) using the pressure-elevation relationship over Antarctica (*147*), and listed in Table S7 – note that the three insolation correction scenarios are listed separately. For each insolation scenario, and for each combination of cores (either WD-EDC or WD-DF) we calculate a lower bound $\Delta\Delta z$ by assuming the entire WAIS-EAIS air content change is solely due to elevation change at WD (with EDC/DF elevation stable), and an upper bound $\Delta\Delta z$ by assuming the entire WAIS-EAIS air content change is solely due to elevation change at EDC/DF (with WD elevation stable) – the reason these two provide an lower and upper bound respectively is because a given TAC change represents a larger fractional change at the higher elevation EDC/DF sites than it does at WD. We also list a "weighted mean", in which we convert the LGM-PI change in WD TAC as if it reflects elevation change at WD, and the LGM-PI change in EDC/DF TAC as if it reflects elevation change at EDC/DF.

We here report a best-estimate $\Delta\Delta z$ of 420 m, with a conservative range of 280 – 590 m; these values are labeled with the letters C, L and U in Table S7, respectively, and given with two significant digits. In order to visually compare our TAC-based estimates to the model-simulated LGM topography anomaly (Fig. 4c), we added a constant elevation change to our TAC-based estimates such that it minimizes the root-mean-square (RMS) offset between the ice sheet model-simulated (Section S3.3) and TAC-based topography anomaly; this yields an LGM elevation anomaly of +310 m, -80 m, and -140 m at WD, EDC and DF, respectively (2 significant digits).

By calculating the RMS offset, we find that the ice sheet simulation by Whitehouse et al. (2012) provides the closest agreement (RMS offset of 13 m) to our TAC-based $\Delta\Delta z$, with a $\Delta\Delta z$ of 403 and 457 m for WD-

EDC and WD-DF, respectively (compare to 388 and 445 m, table S7). The next-best model is ICE-6G, which has an RMS offset of 60 m.

S5 Occam's Razor

Below we list reasons why we believe our reconstructions should be preferred in future interpretation of Antarctic LGM surface climate, rather than the traditional water isotope scaling method in which the modern spatial slope is used.

(1) Complexity: water isotopes are part of a complex system that involves the hemispheric-scale hydrological cycle including sea ice, SST, atmospheric transport, ice topography, etc; several of these changes are poorly constrained. By contrast, firn densification and ice flow are more simple physical systems with only local influences, that can be studied in detail today over a wide range of climatic conditions.

(2) Boundary layer inversion: Small fractional changes to the LGM inversion strength (as simulated in most climate models) complicate the reconstruction of ΔT_S from water isotopes. Both our methods unequivocally reconstruct firn temperature, making the results easier to interpret. A small ΔT_S in central East Antarctica is broadly consistent with water isotope observations via GCM-simulated changes to the LGM inversion (Fig. 4f, Fig. S11).

(3) Consistency: isotope-enabled models simulate LGM-PI temporal slopes that range roughly from 0.3 to 1.4 $‰K^{-1}$ in central East Antarctica (Section S3.5) which would imply a ΔT_S in the range of 4 to 20°C. By contrast, when comparing four different densification models in our Δage-based method, we find a range (largest minus smallest) of reconstructed DT_S of 0.78°C at WD, 1.70°C at EDC, and 1.18°C at DF. The stated 95% confidence range (upper minus lower bound) is 3.8°C at WD, 3.8°C at EDC, and 3.4°C at DF for the borehole method; and 2.6°C at WD, 3.0°C at EDC, and 4.0°C at DF for the Δage method. The borehole- and Δage-based reconstruction methods agree within uncertainty at all sites. It is clear that our reconstruction methods show more consistency and agreement than isotope-enabled GCMs do.

(4) Elevation change: Air content data and ice sheet reconstructions all suggest that the LGM elevation anomaly in West Antarctica is several hundred meter higher than that in central East Antarctica (air content suggests 280 to 590 m); this implies a difference in ΔT_S via the lapse rate. The PMIP4 model ensemble mean finds that ΔT_S at WD minus the ΔT_S in central East Antarctica (here mean of DF and EDC) is around -5.9 ± 2.7°C, in good agreement with our reconstructions (-6.1°C ± 2°C); using traditional water isotope scaling this difference is only -2 to -3°C, which is harder to reconcile with the elevation changes.

(5) Firn data: The traditional interpretation of isotope data ($\Delta T_S \approx$ -9°C) leads to inconsistencies in simulated firn thickness (*105*), despite the fact that firn densification models are very skillful at simulating observed present-day firn density, Δage and $\delta^{15}N$ over a wide range of climatic conditions. Despite efforts, nobody has been able to satisfactorily remove these inconsistencies via changes to densification physics (Section S2.5).

For these reasons, we believe that our solution of reduced ΔT_S in central East Antarctica is the most parsimonious solution: it is consistent with the largest amount of observational and model-based evidence, while requiring the fewest number of assumptions. Following the principle of Occam's razor, this means that a small ΔT_S in central East Antarctica should be the preferred scientific hypothesis.

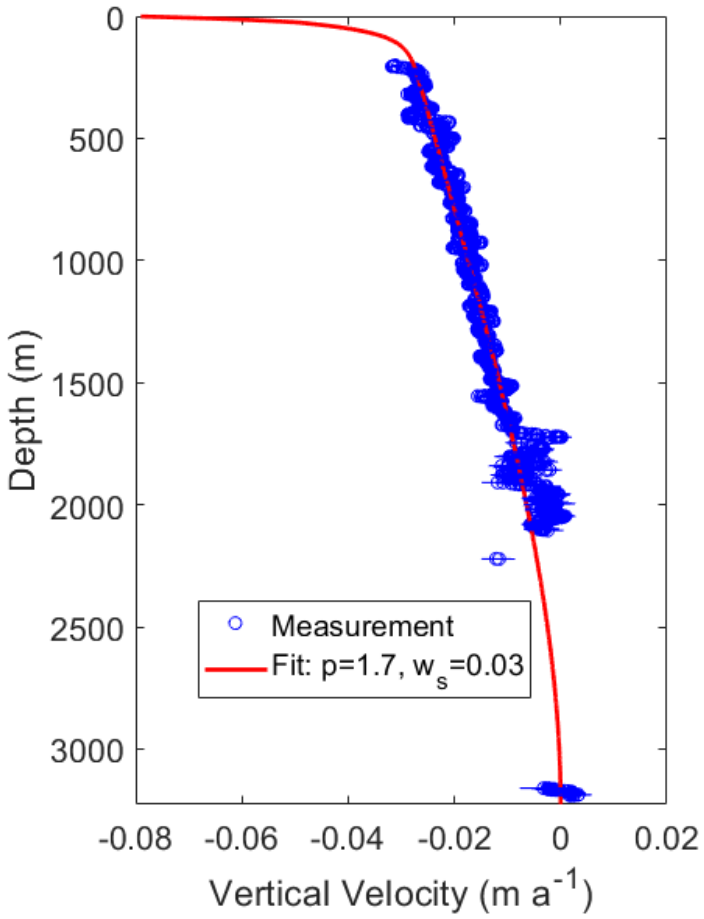

Figure S1: Dome C vertical ice velocity in measurements and models. Example fit for ApRES data with Lliboutry approximation where p and w_s are free parameters. This fit has the ApRES measurements shifted by the mean velocity at depths greater than 3000 m and no basal melt rate applied to the modeled profile. Table S1 provides the fitted values for other combinations of parameters.

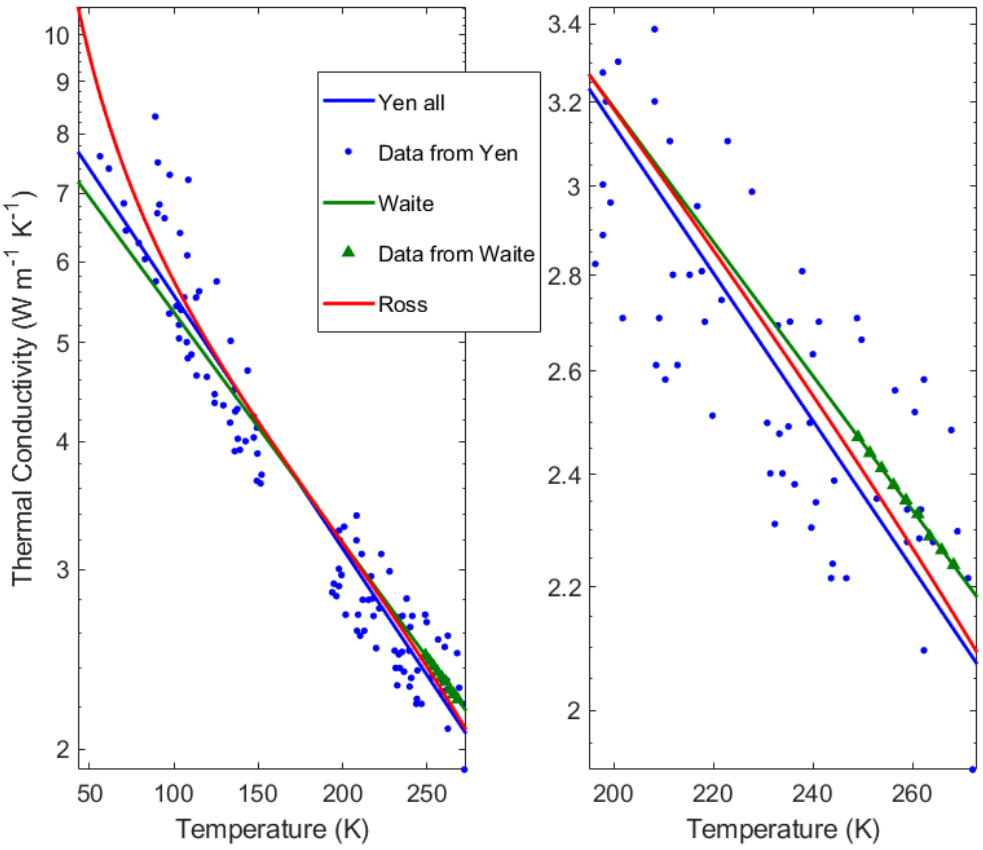

Figure S2: Ice thermal conductivity. Different relationships for the temperature dependence of thermal conductivity. "Yen all" refers to the fit using all temperature data from Yen (1981) which is also in Cuffey and Paterson, 2010 (*33, 34*). "Waite" refers to our fit to the data in Waite et al., 2006 (*45*). "Ross" refers to the fit in Ross et al., 1978 in Table IIIb (*44*). The left panel shows the full range of the data; the right panel shows the same focused on the temperature range relevant to the Dome C ice core.

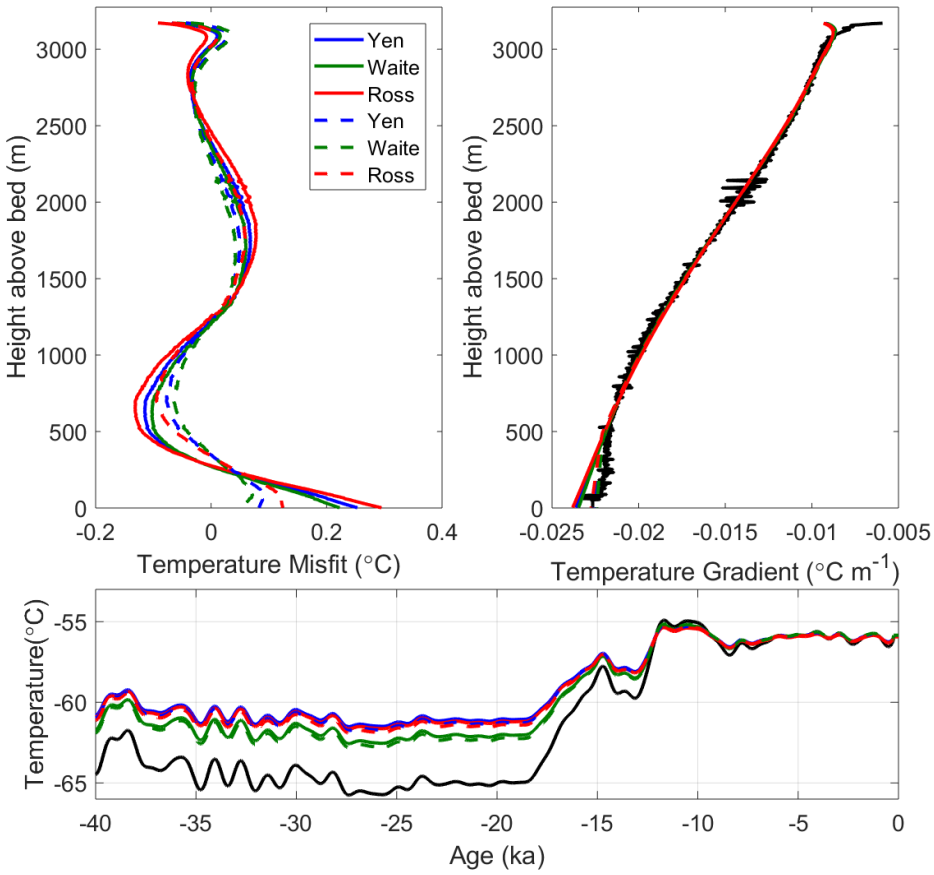

Figure S3: Fitting the Dome C borehole data – sensitivity to thermal conductivity. Upper left panel: Measured minus modeled temperature. Upper right panel: Modeled and measured (black) temperature gradients. Lower panel: Inferred temperature history and temperature history from classical water isotope scaling (black). The solid lines use the thermal conductivity parameterizations from the respective studies (legend in top left panel); the dashed shows the same with a 5% thermal conductivity adjustment applied to the deepest ice as a way to account for the reduced temperature gradient at these depths (top right).

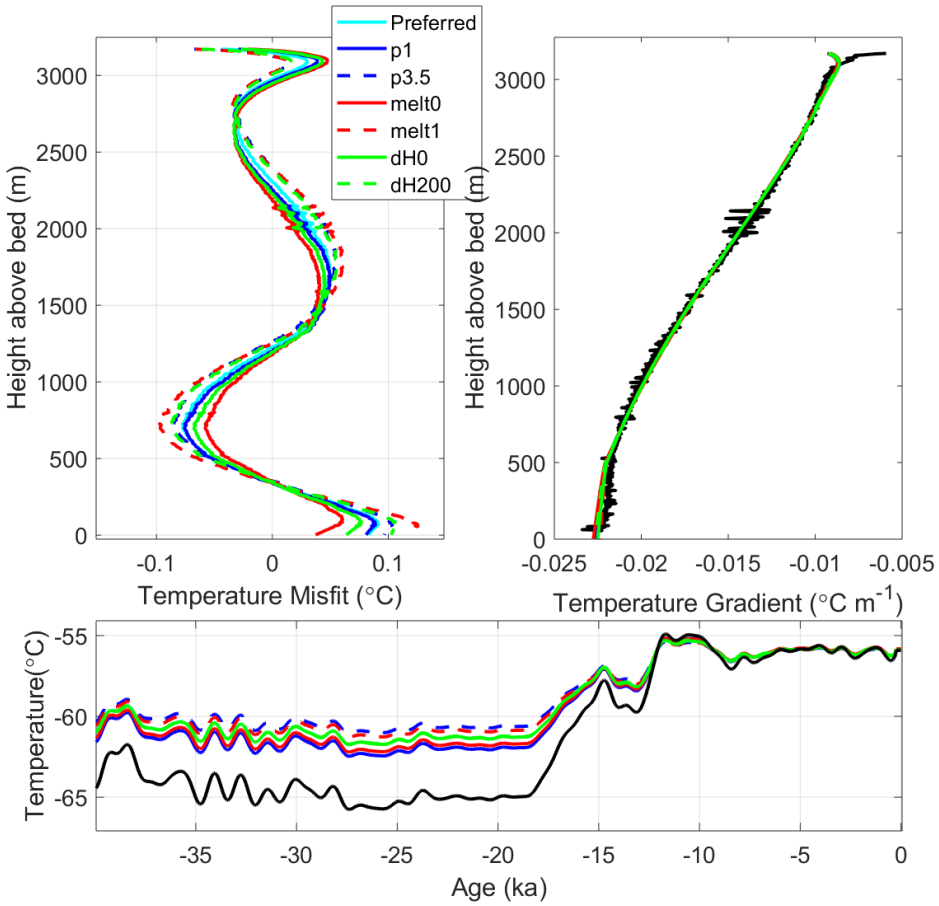

Figure S4: Fitting the Dome C borehole data – sensitivity to ice flow model. Upper left panel: Measured minus modeled temperature. Upper right panel: Modeled and measured (black) temperature gradients. Lower panel: Inferred temperature history and temperature history from classical water isotope scaling (black). Legend is given in the upper left panel, with descriptions given in the text (Section S).

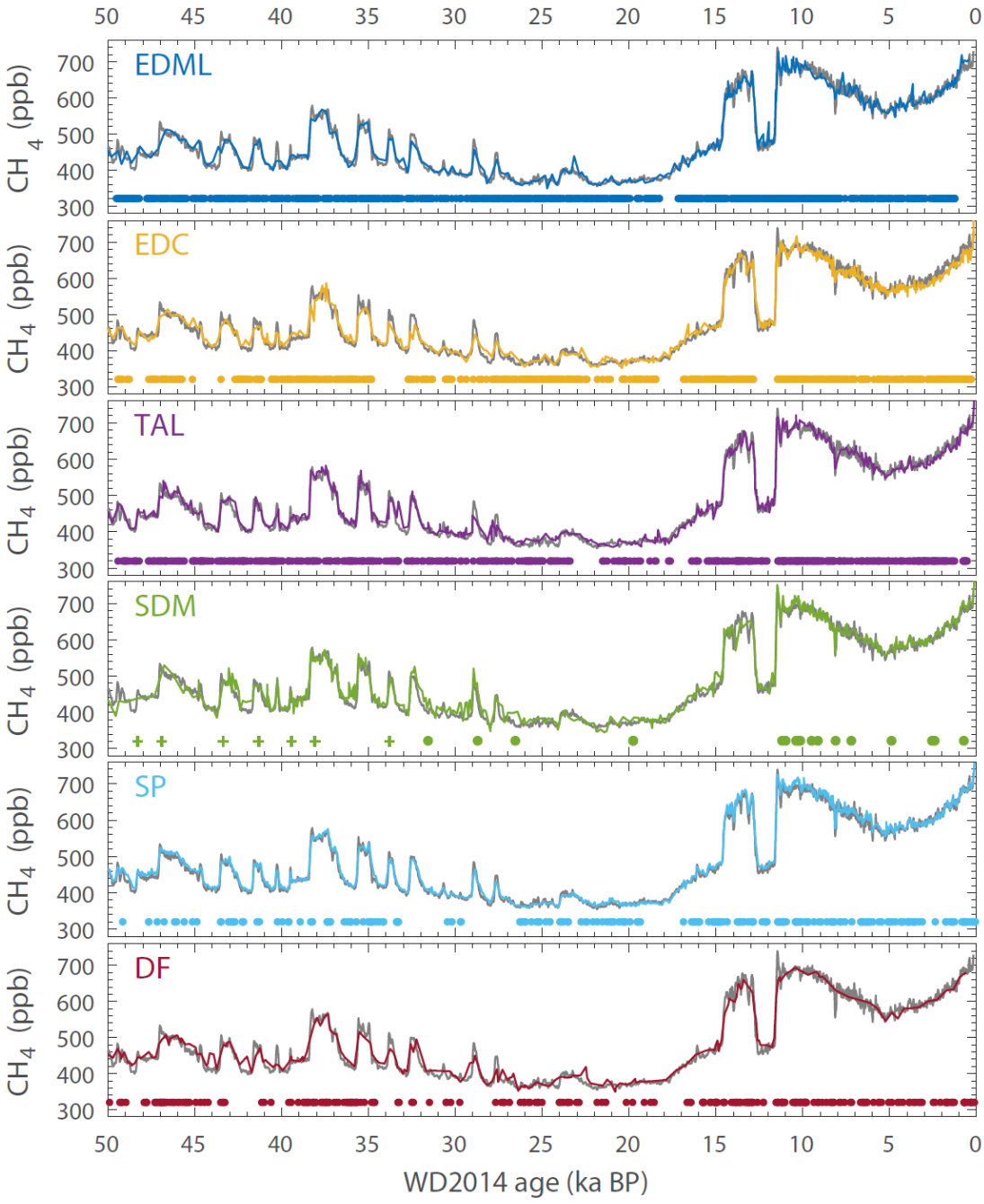

873

874 **Figure S5: Ice core synchronization via atmospheric methane and volcanic markers.** Ice core CH_4 in
875 the various cores (*57, 60, 64-68, 148*) as labeled (colored curve) synchronized to the high-resolution WD
876 CH_4 record (grey curve) on the WD2014 chronology (*30, 31, 80*). Dots represent the ages of volcanic tie
877 points, the + symbols (SDM only) represent ice-ice links based on features matched in the $\delta^{18}O_{ice}$ records.

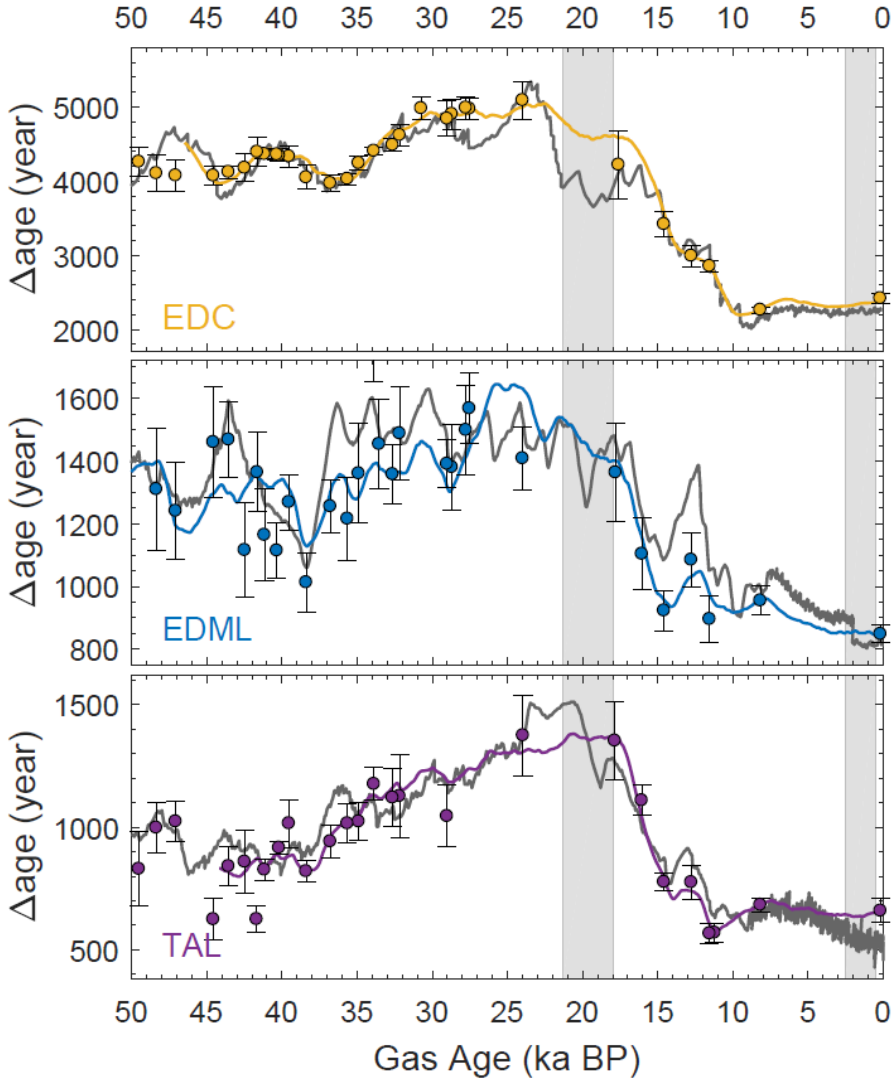

Figure S6: Comparison of Δage to AICC2012. Empirical Δage constraints derived here (dots) together with Δage from firn densification modeling (colored curve) and Δage from the AICC2012 Antarctic Ice Core Chronology (grey curve) for EDC, EDML and TAL (*42*). Note that in the AICC2012 approach Δage is not explicitly modeled; consequently it has abrupt variations (including age inversions) that are likely to be unphysical. The other four sites considered here (WD, SDM, SP and DF) are not part of the AICC2012 framework. Vertical grey shading denotes the LGM and PI periods.

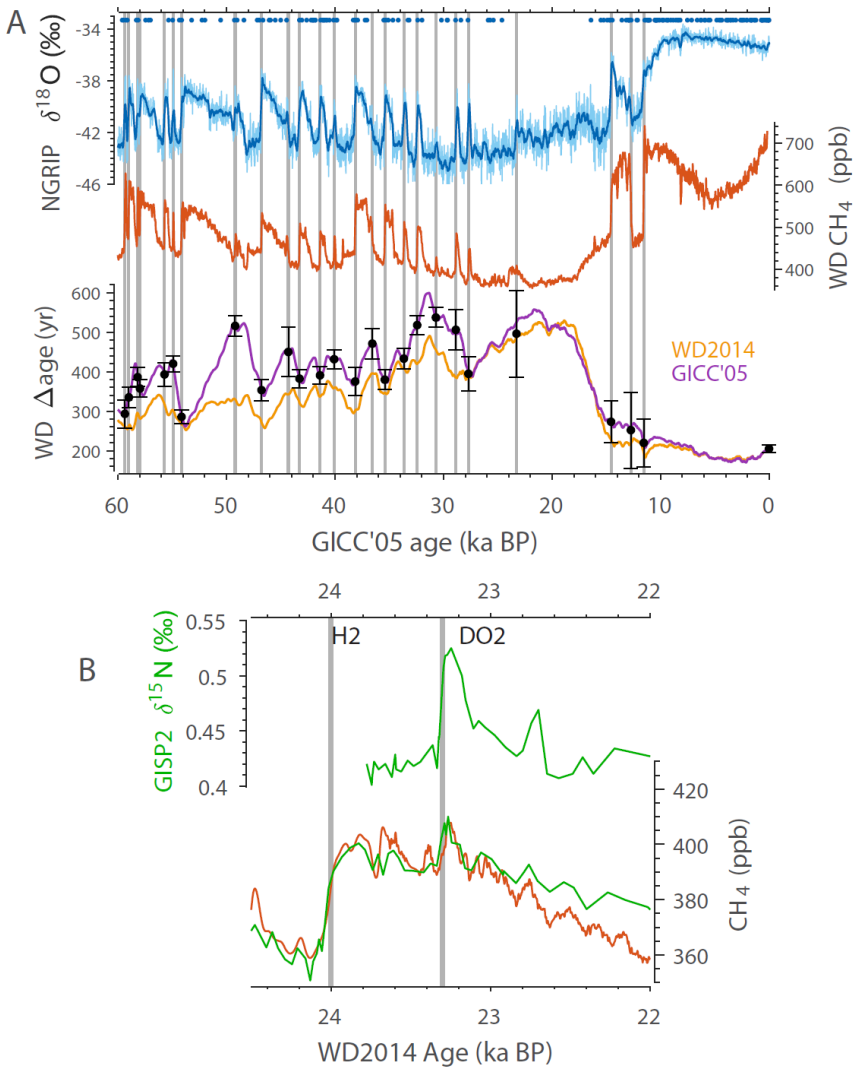

Figure S7: WAIS Divide Δage via bipolar volcanic and CH_4 synchronization. (**a**) Greenland NGRIP $\delta^{18}O$ as a proxy for climate (upper, blue), with the location of bipolar volcanic tie points given as dots; WD atmospheric CH_4 (middle, orange); WD Δage on the WD2014 (*30*) and GICC'05 timescales (bottom, color coded as shown). Black dots with errorbars give the empirical (GICC'05-compatible) WD Δage estimates based on the interpolar synchronization. (**b**) Synchronization at DO2. Top panel: Greenland GISP2 $\delta^{15}N$ (green); Bottom panel: GISP2 CH_4 (green) and WD CH_4 (orange) data. Greenland warming at DO-2 is indicated by GISP2 $\delta^{15}N$, a gas-phase proxy for abrupt Greenland warming (*149*). Greenland DO-2 warming is coincident with a small ~15 ppb CH_4 feature in the GISP2 ice core – the same feature is visible in the WD core. This allows us to assign a GICC'05 gas age to the WD DO2 CH_4 feature, using the DO-2 GICC'05 ice age. While the Heinrich H-2 CH_4 feature is more pronounced than the DO-2 CH_4 feature, it cannot be used to synchronize WD to the GICC'05 ice chronology because the H-events are not recorded in the Greenland ice phase. The H-2 CH_4 feature is used for synchronizing Antarctic CH_4 records from various cores, however (Fig. S5).

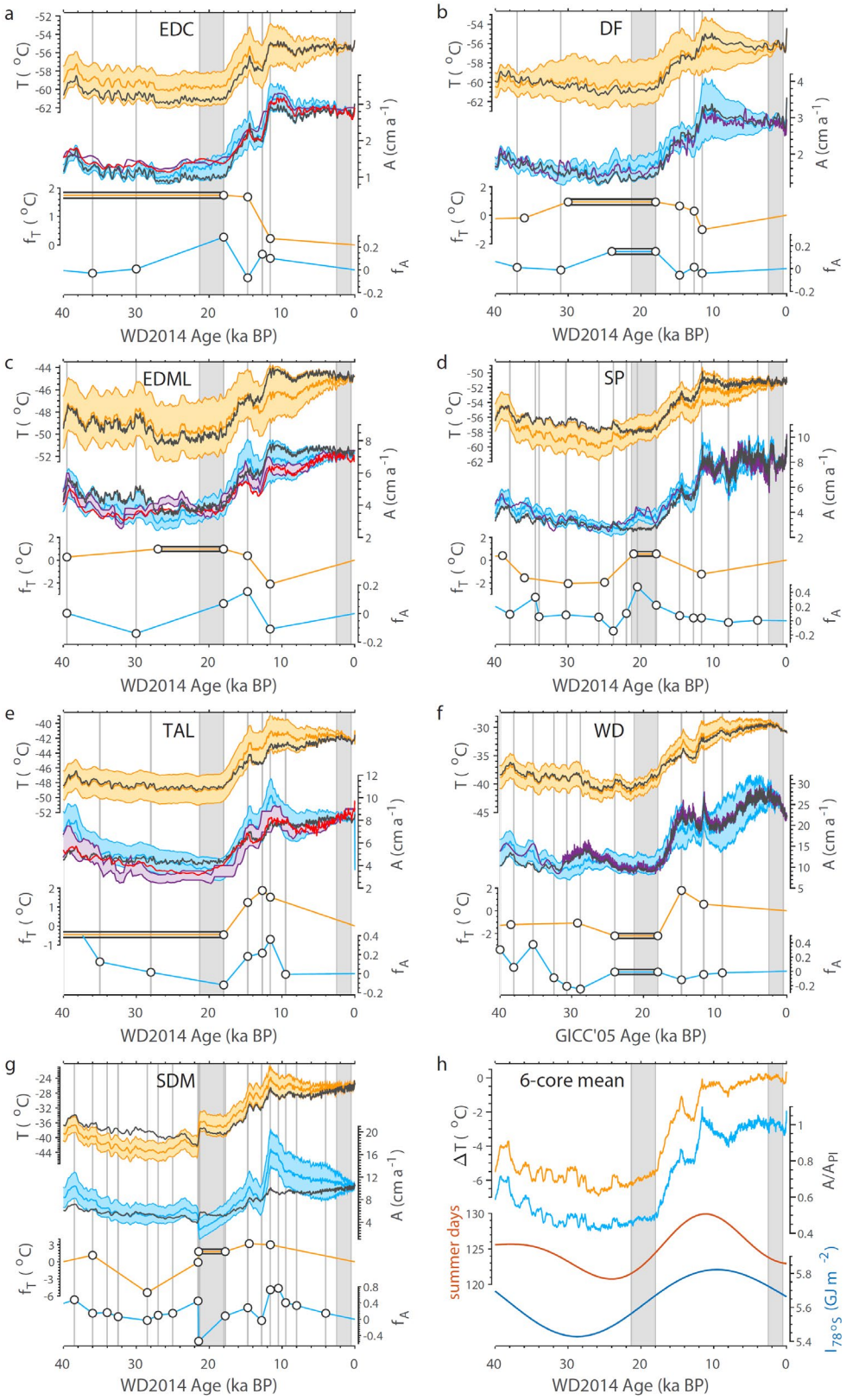

Figure S8: Firn-based accumulation rate and temperature reconstructions. (**a**) EDC; (**b**) DF; (**c**) EDML; (**d**) SP; (**e**) TAL; (**f**) WD; (g) SDM. The initial guesses $T_{init}(t)$ and $A_{init}(t)$ are shown in grey; the

$T_{site}(t)$ and $A_{site}(t)$ reconstructions in orange and blue, respectively, using the Monte Carlo estimation (Section S2.4) with the envelope giving the 95% confidence range and the center line giving the distribution mean. The high-frequency T and A variability comes from the $\delta^{18}O$, not from the optimization method. The purple curves give accumulation estimates from de-strained layer thickness in the core, the red curves give the accumulation estimates from the AICC2012 chronology (*42*). The $f_T(t)$ and $f_A(t)$ modification functions are shown below in orange and blue, respectively, with the control points and intervals shown as white circles and grey bars, respectively. (**h**) Six-core average T and A as anomalies relative to the PI. SDM is withheld from the averaging because the abrupt 21ka feature is likely a local glaciological effect, and not representative of Antarctic climate. Summer duration (red, days with insolation over 250 Wm^{-2}) and annually integrated insolation (blue) are both at 78°S (mean core latitude).

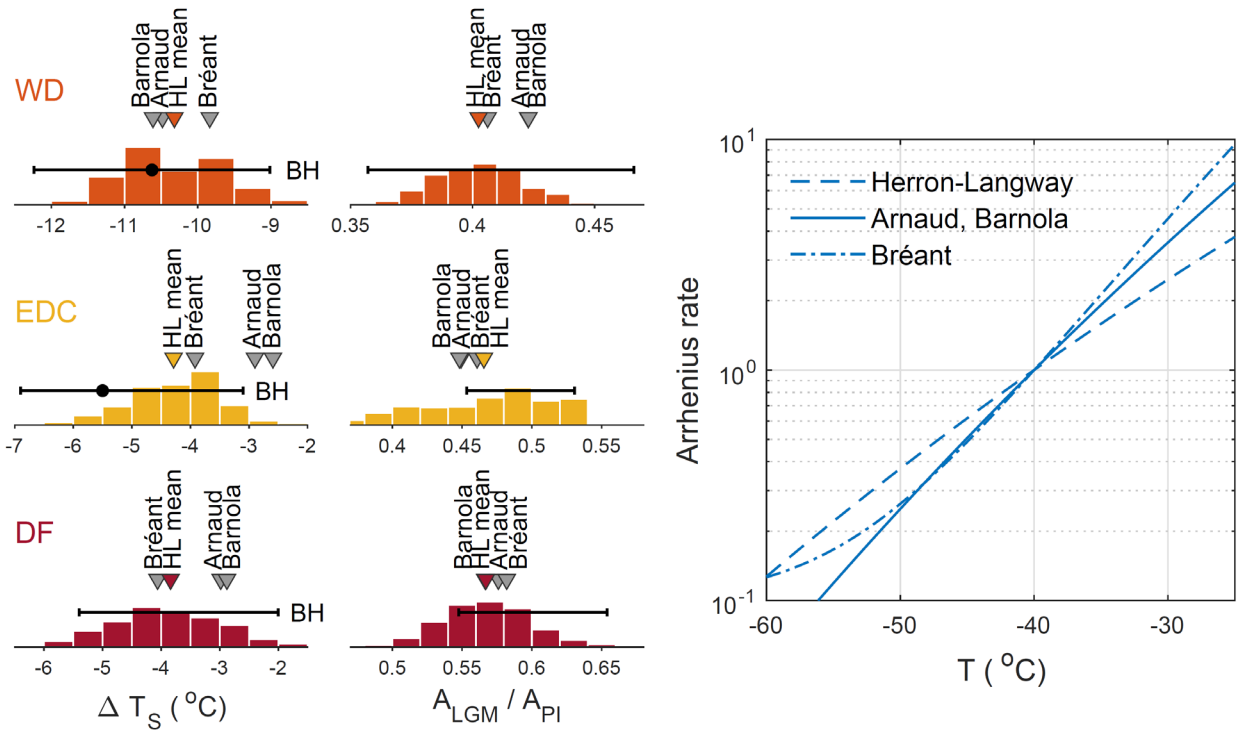

Fig. S9. Firn-based climate reconstructions – a model comparison. Histograms: ice core temperature and accumulation reconstructions for the WD, EDC and DF sites. Histograms give the spread in the Herron-Langway Monte Carlo sensitivity study (distribution mean indicated with colored triangles). Results from the Arnaud (*88, 103*), Barnola (*20, 87*) and Bréant (*89*) firn densification models are indicated by the grey triangles as marked. Black data and horizontal error bars give the range of borehole temperatures (marked BH), and the range of accumulation rates consistent with the ice flow model uncertainty used in the borehole temperature reconstructions. Right panel: plots of the Arrhenius-type activation energy term for the second stage of firn densification in the firn models. The Arrhenius term has the form exp(-Q/RT), with R the gas constant, T the Kelvin temperature and Q the activation energy; the Herron-Langway model uses Q_{HL} = 42.6 kJ/mol; the Arnaud and Barnola models use $Q_A = Q_B$ = 60kJ/mol; the Bréant model uses a weighted sum of three activation energies (Q_1 = 110 kJ/mol, Q_2 = 75 kJ/mol, Q_3 = 1.5 kJ/mol). All values are normalized to unit Arrhenius rate at -40°C.

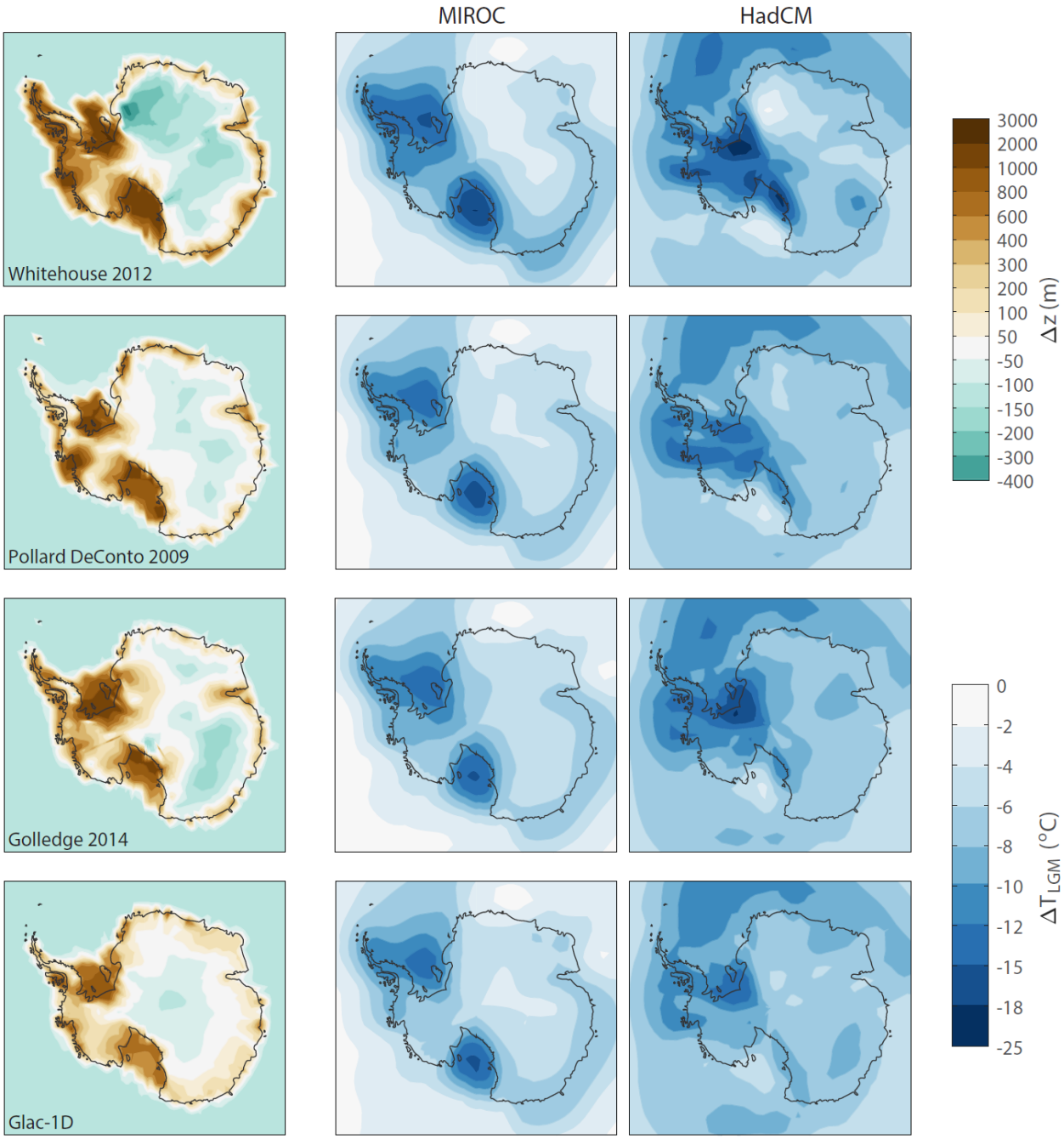

928

929 **Fig S10: Climate model ice sheet sensitivity study (continued on next page).** Left panels: Antarctic
930 LGM-PI surface topography anomalies used to force the climate model simulations. Topographies as
931 indicated from refs (*29, 50, 116, 121-125*). Note that the anomalies are shown relative to the modern geoid,
932 and as such the LGM sea level drop appears as a negative height anomaly over the oceans. Middle and right
933 panels: Antarctic cooling DT_S simulated in the MIROC and HadCM AOGCMs, respectively, using the
934 topographic forcing shown in the left panels. The upper five topographies are used in the analyses of the
935 main manuscript; the Ice-5G and PMIP3 topographies are shown here for comparison purposes only.

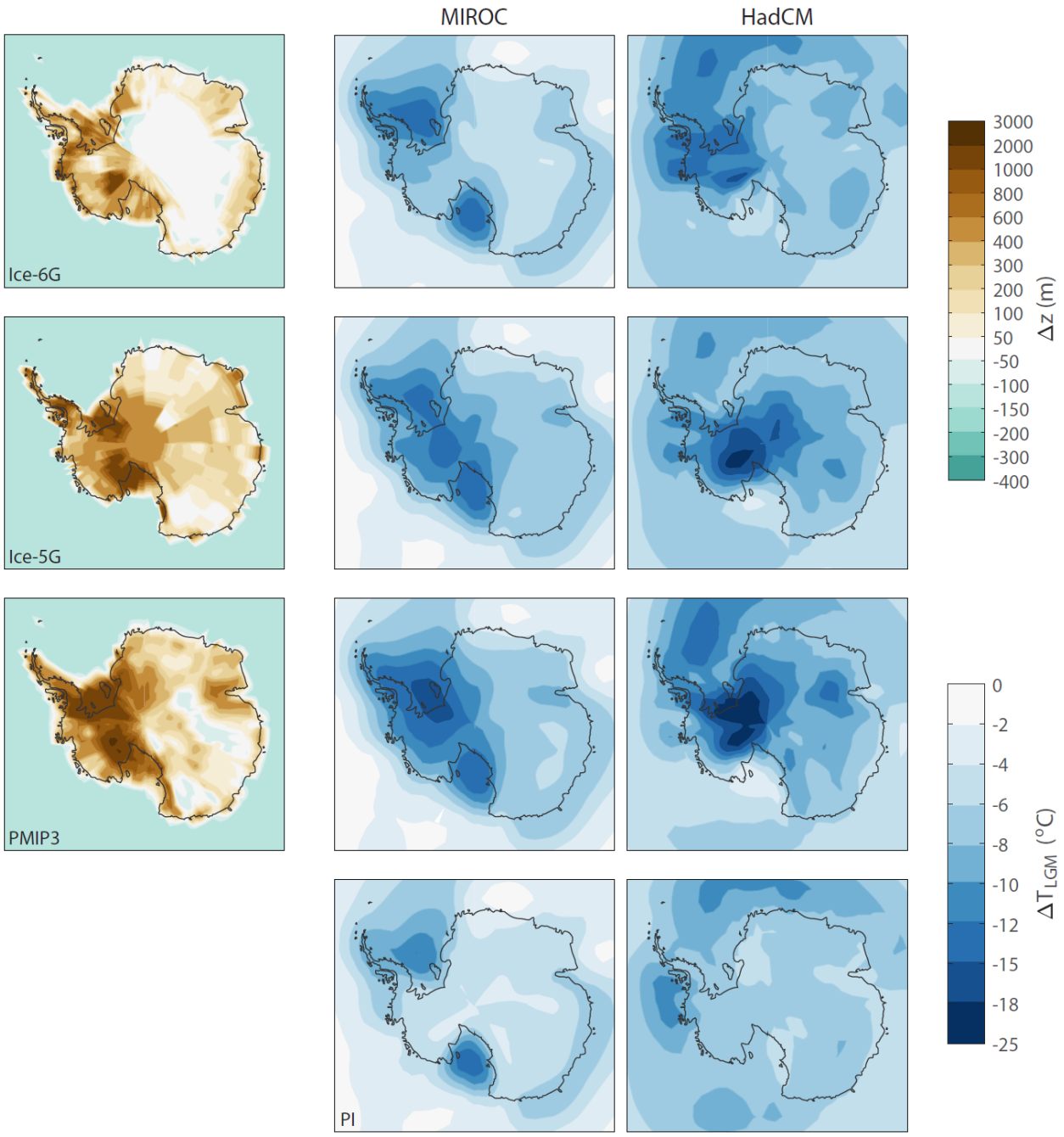

936

937 **Fig. S10 (continued).** Bottom row shows the Pre-industrial ice sheet forcing.

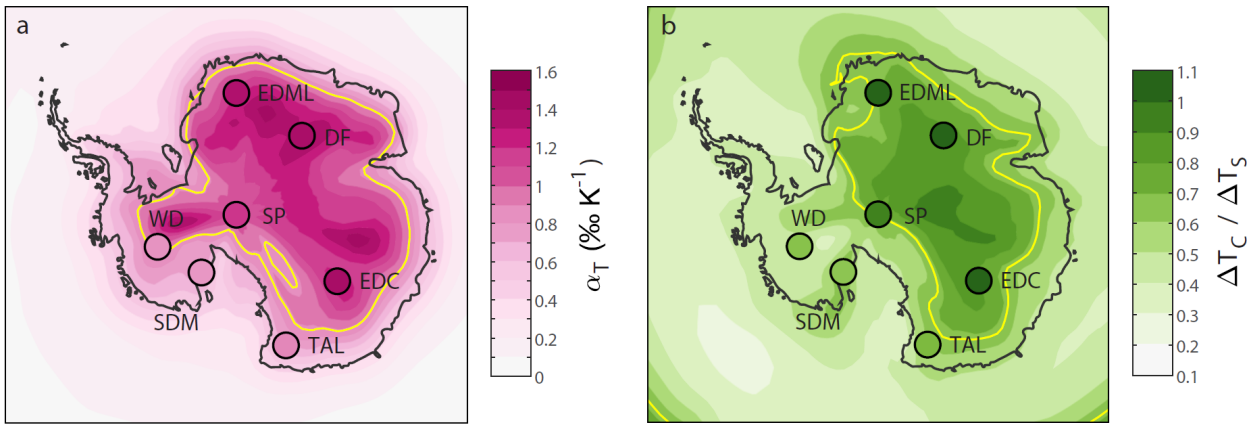

938

939 **Fig S11: Changes to the inversion strength.** (**a**) Map of the LGM-preindustrial temporal isotope slope in
940 isotope-enabled CESM simulations (shading), with the same based on the reconstructed ΔT_S (dots). Data
941 and simulations are corrected for mean-ocean $\delta^{18}O$. The yellow contour line traces the modern spatial slope
942 value of 0.8 ‰ K^{-1} (*2*). (**b**) Map of the ratio ΔT_C / ΔT_S (both calculated as the LGM-preindustrial change)
943 in the CESM simulations (shading), with the same based on the data-based reconstructions (dots). The 500
944 hPa temperature is used as a proxy for T_C in CESM; this is the height with the warmest tropospheric
945 temperatures over interior Antarctica. The yellow contour line follows the modern spatial value 0.65 (*2*).

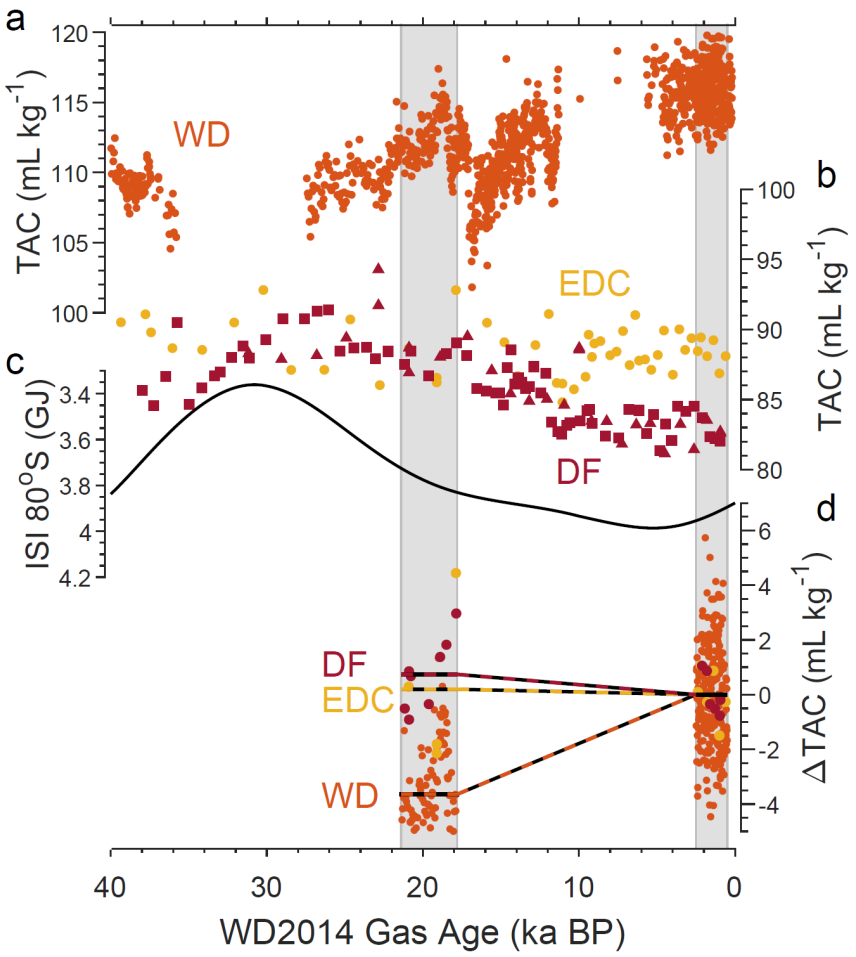

946

947 **Fig S12: Total air content records and site elevation change. (a)** WAIS Divide total air content data
948 (orange). **(b)** EPICA Dome C total air content data (yellow) and Dome Fuji total air content data from the
949 STAN setup (red triangles) and gas chromatography setup (red squares). **(c)** Integrated summer insolation
950 at 80°S, a key control on ice core air content (*22*). **(d)** LGM-PI changes in TAC at the three sites, with DF
951 and EDC showing a decrease in TAC, and WD showing an increase in TAC through time. These changes
952 can be interpreted in terms of relative surface elevation change (see text). All air content data are reported
953 in mL air (at standard temperature and pressure) per kg of ice.

954

Table S1: Fitting the Lliboutry equation to the ApRES data. Fit uses Equation S2 where ws is the surface vertical velocity which is the sum of accumulation rate and ice thickness change. The ApRES data are shown in Fig. S1.

ApRES uniform adjustment (m a^{-1})	**melt rate in model fit (m a^{-1})**	***p***	**w_s (m a^{-1})**
0	0	3.2	0.032
0	-0.0005	2.85	0.032
0	-0.0022	1.2	0.033
0.0022	0	1.7	0.030
0.0015 (0.0022 to 0.0005)	-0.0005	1.35	0.031
	Average	**2.06**	**0.032**

Table S2: The effect of thermal conductivity on reconstructed ΔT_S at EDC. We find the temperature history (and ΔT_S) that provides the best fit to the EDC borehole data using three different parameterizations of thermal conductivity. We either applied no adjustment to basal thermal conductivities, or up to 5% increased conductivities (as marked). See Section S1.2.1 for more information. All scenarios use our best estimate ice flow model.

	No Basal Adjustment		**Basal Adjustment up to 5%**	
	ΔT_S (°C)	**RMS (°C)**	**ΔT_S (°C)**	**RMS (°C)**
Yen (1981)	-5.04	0.0707	-5.29	0.0431
Waite (2006)	-6.01	0.0627	-6.27	0.0359
Ross (1978)	-5.14	0.0817	-5.39	0.0533
Average (all 6)	**-5.52**			
Range (all 6)	**1.23**			

Table S4: Uncertainty estimation for EDC borehole reconstruction.

p value	2	4	4	4	7	7	7	15	15	15
onset (ka)	none	10	6	2	10	6	2	10	6	2
ΔT_S (°C)	-5.29	-4.85	-4.73	-4.52	-4.51	-4.27	-3.91	-4.14	-3.80	-3.27
ΔT_S change		0.44	0.56	0.77	0.78	1.02	1.38	1.15	1.49	2.02
RMS	.0431	.0468	.0481	.0496	.0505	.0539	.0598	.0553	.0623	.0762
RMS change		.0037	.0050	.0065	.0074	.0108	.0167	.0122	.0192	.0331

Average ΔT_S change	1.07°C
Range ΔT_S change	2.02°C

Table S4: Uncertainty estimation for EDC borehole reconstruction. The values given represent the uni-directional uncertainty; the full uncertainty range (interpreted as a 95% confidence interval) equals twice the values listed. The full ΔT_S uncertainty range stated in the manuscript equals 3.1 to 6.9°C, or 5.0 ±1.9°C.

	ΔT_S uncertainty (°C)
Vertical velocity profile (p)	0.68
Basal melt rate	0.37
Ice thickness history	0.10
Time-variable vertical profile (p)	1.01
Ice flow Total	**1.3**
Thermal conductivity (Table S2)	**0.6**
Total Uncertainty (Flow + thermal)	**1.9**

Table S5: Firn densification model input parameters and ranges. Preferred model input parameters used in the dynamical Herron-Langway firn densification model with their range (noted with σ) used in the Monte Carlo sensitivity study. CZ is the convective zone thickness; ρ_0 the firn surface density; ρ_{diff} expresses the density difference between the lock-in (r_{LI}) where gases are effectively isolated from the atmosphere, and the close-off (r_{LI}) which is known from parameterizations (*97*), such that $\rho_{LI} = \rho_{CO}$-ρ_{diff}; H is the ice sheet thickness; GHF is the geothermal heat flux – note that the model was not optimized to reconstruct this parameter and we advise against using it in other applications.

Site	CZ [m]	σ_1 (CZ) [m]	σ_2 (CZ) [m]	ρ_0 [kg m^{-3}]	σ (ρ_0) [kg m^{-3}]	ρ_{diff} [kg m^{-3}]	$\sigma(\rho_{diff})$ [kg m^{-3}]	GHF [mW m^{-2}]	H [m]	α_{init} [‰K^{-1}]
EAIS										
EDC	0.0[a]	2.0	5.0	340	50	4.0	4.0	48	3275	1.1
DF	4.0[b]	2.0	5.0	335	50	3.0	4.0	54	3038	1.2
EDML	2.0[c]	2.0	5.0	320	50	5.0	4.0	50	2590	1.15
TAL	5.0[d]	2.0	5.0	320	50	9.0	4.0	62	1620	0.95
SP	6.0[e]	2.0	5.0	380	50	15	4.0	56	2600	1.1
WAIS										
WD	3.5[f]	2.0	5.0	420	50	10	4.0	n/a[g]	1000[g]	0.88
SDM	2.0[h]	2.0	5.0	340	50	3.5	4.0	72	1004	0.7

[a] See ref. (*150*)
[b] Lower bound from model fitting in ref. (*151*)
[c] Based on EDML firn air data (*152*)
[d] Generic value used owing to lack of data
[e] Firn-based estimates suggest the CZ is around 3 m at SP (*153*); increased here to fit ice core $\delta^{15}N$ data
[f] See ref. (*154*)
[g] Due to the high accumulation rates at WD, the geothermal heat flux does not meaningfully penetrate into the firn column and only the upper 1000m are simulated in accordance with ref. (*30*).
[h] See ref. (*153*).

Table S6: Firn densification model input parameters for alternative firn model physics. Preferred model input parameters used in the various firn densification models. CZ is the convective zone thickness; ρ_0 the firn surface density; ρ_{diff} expresses the density difference between the lock-in (r_{LI}) where gases are effectively isolated from the atmosphere, and the close-off (r_{LI}) which is known from parameterizations (*97*), such that $\rho_{LI} = \rho_{CO}-\rho_{diff}$; H, GHF and α_{init} are as in Table S5 and identical for the different models.

Site and Model	CZ [m]	ρ_0 [kg m^{-3}]	ρ_{diff} [kg m^{-3}]
WDC			
Herron-Langway	3.5	420	10
Arnaud	3.5[a]	390	-2.0
Barnola	3.5[a]	420	10
Bréant	3.5[a]	420	6.0
EDC			
Herron-Langway	0.0	340	4.0
Arnaud	1.0[b]	340	-2.0
Barnola	1.0[b]	340	4.0
Bréant	1.0[b]	340	1.0
DF			
Herron-Langway	4.0	335	3.0
Arnaud	4.0	335	-3.0
Barnola	4.0	335	3.0
Bréant	4.0	335	-1.0

Table S7: Relative elevation changes inferred from total air content records. All elevation changes are expressed as relative WAIS (WD) minus EAIS (EDC, DF) LGM elevation changes, and not absolute changes relative to the geoid. So a value of +400 m could for example indicate a 300 m elevation increase at WD, and a 100 m of elevation decrease at EDC/DF, or for example a 500m elevation increase at WD and a 100m elevation increase at EDC/DF. See the text (Section S4) for details. The values marked with letters C, L, and U, are used as the central estimate, lower bound and upper bound, respectively, reported in the main manuscript (in two significant digits).

	Lower bound [m]	Weighted mean [m]	Upper bound [m]
No insolation correction			
WD-EDC	418	496	516
WD-DF	453	563	588 U
mean	436	530	552
Best-estimate insolation correction			
WD-EDC	346	388	429
WD-DF	380	445	496
mean	363	417 C	462
2 × best-estimate insolation correction			
WD-EDC	275 L	278	342
WD-DF	308	325	404
mean	291	302	373

Supplementary references and notes

32. L. Lliboutry, A critical review of analytical approximate solutions for steady state velocities and temperatures in cold ice-sheets. *Gletscherkd. Glazialgeol* **15**, 135–148 (1979).
33. K. M. Cuffey, W. S. B. Paterson, *The physics of glaciers, 4th edition*. (Butterworth-Heinemann, Oxford, UK, 2010), pp. 693.
34. Y.-C. Yen, *Review of thermal properties of snow, ice, and sea ice*. (US Army, Corps of Engineers, Cold Regions Research and Engineering Laboratory, 1981), vol. 81.
35. N. Calonne *et al.*, Thermal Conductivity of Snow, Firn, and Porous Ice From 3-D Image-Based Computations. *Geophys. Res. Lett.* **46**, 13079-13089 (2019).
36. G. D. Clow, R. W. Saltus, E. D. Waddington, A new high-precision borehole-temperature logging system used at GISP2, Greenland, and Taylor Dome, Antarctica. *J. Glaciol.* **42**, 576-584 (1996).
37. K. W. Nicholls *et al.*, A ground-based radar for measuring vertical strain rates and time-varying basal melt rates in ice sheets and shelves. *J. Glaciol.* **61**, 1079-1087 (2015).
38. J. Kingslake *et al.*, Full-depth englacial vertical ice sheet velocities measured using phase-sensitive radar. *Journal of Geophysical Research: Earth Surface* **119**, 2014JF003275 (2014).
39. F. Parrenin *et al.*, 1-D-ice flow modelling at EPICA Dome C and Dome Fuji, East Antarctica. (2007).
40. C. Buizert *et al.*, Abrupt ice-age shifts in southern westerly winds and Antarctic climate forced from the north. *Nature* **563**, 681-685 (2018).
41. L. Bazin *et al.*, An optimized multi-proxy, multi-site Antarctic ice and gas orbital chronology (AICC2012): 120–800 ka. *Clim. Past* **9**, 1715-1731 (2013).
42. D. Veres *et al.*, The Antarctic ice core chronology (AICC2012): an optimized multi-parameter and multi-site dating approach for the last 120 thousand years. *Clim. Past* **9**, 1733-1748 (2013).
43. R. Uemura *et al.*, Asynchrony between Antarctic temperature and CO2 associated with obliquity over the past 720,000 years. *Nature Communications* **9**, 961 (2018).
44. R. Ross, P. Andersson, G. Bäckström, Effects of H and D order on the thermal conductivity of ice phases. *The Journal of Chemical Physics* **68**, 3967-3972 (1978).
45. W. F. Waite, L. Y. Gilbert, W. J. Winters, D. H. Mason, Estimating thermal diffusivity and specific heat from needle probe thermal conductivity data. *Review of Scientific Instruments* **77**, 044904 (2006).
46. G. Durand *et al.*, in *Physics of Ice Core Records II,* T. Hondoh, Ed. (Institute of Low Temperature Science, Hokkaido University, 2009), pp. 91-105.
47. L. Bonales, A. C. Rodríguez, P. Sanz, Thermal conductivity of ice prepared under different conditions. *International journal of food properties* **20**, 610-619 (2017).
48. C. F. Raymond, Deformation in the vicinity of ice divides. *J. Glaciol.* **29**, 357-373 (1983).
49. R. M. DeConto, D. Pollard, Contribution of Antarctica to past and future sea-level rise. *Nature* **531**, 591-597 (2016).
50. N. R. Golledge *et al.*, Antarctic contribution to meltwater pulse 1A from reduced Southern Ocean overturning. *Nat Commun* **5**, (2014).
51. K. Matsuoka *et al.*, Antarctic ice rises and rumples: Their properties and significance for ice-sheet dynamics and evolution. *Earth-Sci. Rev.* **150**, 724-745 (2015).
52. D. Dahl-Jensen *et al.*, Past Temperatures Directly from the Greenland Ice Sheet. *Science* **282**, 268-271 (1998).
53. K. Kawamura *et al.*, State dependence of climatic instability over the past 720,000 years from Antarctic ice cores and climate modeling. *Science Advances* **3**, (2017).

54. J. P. Severinghaus, R. Beaudette, M. A. Headly, K. Taylor, E. J. Brook, Oxygen-18 of O2 Records the Impact of Abrupt Climate Change on the Terrestrial Biosphere. *Science* **324**, 1431-1434 (2009).
55. D. A. Winski *et al.*, The SP19 chronology for the South Pole Ice Core – Part 1: volcanic matching and annual layer counting. *Clim. Past* **15**, 1793-1808 (2019).
56. E. Capron *et al.*, Glacial–interglacial dynamics of Antarctic firn columns: comparison between simulations and ice core air-δ15N measurements. *Clim. Past* **9**, 983-999 (2013).
57. K. Kawamura, Tohoku University, Japan, (2000).
58. M. A. Headly, University of California San Diego, (2008).
59. J. P. Severinghaus, A. Grachev, B. Luz, N. Caillon, A method for precise measurement of argon 40/36 and krypton/argon ratios in trapped air in polar ice with applications to past firn thickness and abrupt climate change in Greenland and at Siple Dome, Antarctica. *Geochim. Cosmochim. Acta* **67**, 325-343 (2003).
60. L. Loulergue *et al.*, Orbital and millennial-scale features of atmospheric CH4 over the past 800,000 years. *Nature* **453**, 383-386 (2008).
61. A. Schilt *et al.*, Glacial-interglacial and millennial-scale variations in the atmospheric nitrous oxide concentration during the last 800,000 years. *Quat. Sci. Rev.* **In Press, Corrected Proof**, (2009).
62. A. M. Seltzer *et al.*, Does δ18O of O2 record meridional shifts in tropical rainfall? *Clim. Past* **13**, 1323-1338 (2017).
63. R. Spahni *et al.*, Atmospheric methane and nitrous oxide of the late Pleistocene from Antarctic ice cores. *Science* **310**, 1317-1321 (2005).
64. E. J. Brook *et al.*, Timing of millennial-scale climate change at Siple Dome, West Antarctica, during the last glacial period. *Quat. Sci. Rev.* **24**, 1333-1343 (2005).
65. J. Ahn, E. J. Brook, Siple Dome ice reveals two modes of millennial CO2 change during the last ice age. *Nat Commun* **5**, (2014).
66. J. W. Yang, J. Ahn, E. J. Brook, Y. Ryu, Atmospheric methane control mechanisms during the early Holocene. *Clim. Past* **13**, 1227-1242 (2017).
67. J. Ahn, E. J. Brook, C. Buizert, Response of atmospheric CO2 to the abrupt cooling event 8200 years ago. *Geophys. Res. Lett.* **41**, 604–609 (2014).
68. J. Ahn, E. J. Brook, A. Schmittner, K. Kreutz, Abrupt change in atmospheric CO2 during the last ice age. *Geophys. Res. Lett.* **39**, L18711 (2012).
69. EPICA-Community-Members, One-to-one coupling of glacial climate variability in Greenland and Antarctica. *Nature* **444**, 195-198 (2006).
70. WAIS-Divide-Project-Members, Onset of deglacial warming in West Antarctica driven by local orbital forcing. *Nature* **500**, 440-444 (2013).
71. WAIS-Divide-Project-Members, Precise interpolar phasing of abrupt climate change during the last ice age. *Nature* **520**, 661-665 (2015).
72. B. Stenni *et al.*, Expression of the bipolar see-saw in Antarctic climate records during the last deglaciation. *Nat. Geosci.* **4**, 46-49 (2011).
73. E. J. Steig *et al.*, South Pole high resolution ice core water stable isotope record for dD, d18O. *U.S. Antarctic Program (USAP) Data Center*, (2020).
74. E. J. Steig *et al.*, Recent climate and ice-sheet changes in West Antarctica compared with the past 2,000 years. *Nature Geosci* **6**, 372-375 (2013).
75. B. R. Markle *et al.*, Global atmospheric teleconnections during Dansgaard-Oeschger events. *Nature Geosci* **10**, 36-40 (2017).
76. C. Waelbroeck *et al.*, Sea-level and deep water temperature changes derived from benthic foraminifera isotopic records. *Quat. Sci. Rev.* **21**, 295-305 (2002).

77. T. J. Fudge, K. C. Taylor, E. D. Waddington, J. J. Fitzpatrick, H. Conway, Electrical stratigraphy of the WAIS Divide ice core: Identification of centimeter-scale irregular layering. *Journal of Geophysical Research: Earth Surface* **121**, 2016JF003845 (2016).
78. N. W. Dunbar, A. V. Kurbatov, Tephrochronology of the Siple Dome ice core, West Antarctica: correlations and sources. *Quat. Sci. Rev.* **30**, 1602-1614 (2011).
79. N. W. Dunbar *et al.*, New Zealand supereruption provides time marker for the Last Glacial Maximum in Antarctica. *Scientific Reports* **7**, 12238 (2017).
80. R. H. Rhodes *et al.*, Enhanced tropical methane production in response to iceberg discharge in the North Atlantic. *Science* **348**, 1016-1019 (2015).
81. S. Fujita, F. Parrenin, M. Severi, H. Motoyama, E. W. Wolff, Volcanic synchronization of Dome Fuji and Dome C Antarctic deep ice cores over the past 216 kyr. *Clim. Past* **11**, 1395-1416 (2015).
82. M. Severi *et al.*, Synchronisation of the EDML and EDC ice cores for the last 52 kyr by volcanic signature matching. *Clim. Past* **3**, 367-374 (2007).
83. M. Severi, R. Udisti, S. Becagli, B. Stenni, R. Traversi, Volcanic synchronisation of the EPICA-DC and TALDICE ice cores for the last 42 kyr BP. *Clim. Past* **8**, 509-517 (2012).
84. A. Svensson *et al.*, Bipolar volcanic synchronization of abrupt climate change in Greenland and Antarctic ice cores during the last glacial period. *Clim. Past Discuss.* **2020**, 1-28 (2020).
85. J. L. Rosen *et al.*, An ice core record of near-synchronous global climate changes at the Bolling transition. *Nat. Geosci.* **7**, 459-463 (2014).
86. M. Baumgartner *et al.*, NGRIP CH4 concentration from 120 to 10 kyr before present and its relation to a δ15N temperature reconstruction from the same ice core. *Clim. Past* **10**, 903-920 (2014).
87. J. M. Barnola, P. Pimienta, D. Raynaud, Y. S. Korotkevich, CO2-climate relationship as deduced from the Vostok ice core: a re-examination based on new measurements and on a re-evaluation of the air dating. *Tellus* **43**, 83-90 (1991).
88. C. Goujon, J. M. Barnola, C. Ritz, Modeling the densification of polar firn including heat diffusion: Application to close-off characteristics and gas isotopic fractionation for Antarctica and Greenland sites. *J. Geophys. Res.* **108**, 18 (2003).
89. C. Bréant, P. Martinerie, A. Orsi, L. Arnaud, A. Landais, Modelling firn thickness evolution during the last deglaciation: constraints on sensitivity to temperature and impurities. *Clim. Past* **13**, 833-853 (2017).
90. P. Kindler *et al.*, Temperature reconstruction from 10 to 120 kyr b2k from the NGRIP ice core. *Clim. Past* **10**, 887-902 (2014).
91. C. Huber *et al.*, Isotope calibrated Greenland temperature record over Marine Isotope Stage 3 and its relation to CH(4). *Earth Planet. Sci. Lett.* **243**, 504-519 (2006).
92. J. Schwander, B. Stauffer, AGE DIFFERENCE BETWEEN POLAR ICE AND THE AIR TRAPPED IN ITS BUBBLES. *Nature* **311**, 45-47 (1984).
93. S. O. Rasmussen *et al.*, A first chronology for the North Greenland Eemian Ice Drilling (NEEM) ice core. *Clim. Past* **9**, 2713-2730 (2013).
94. I. Seierstad *et al.*, Consistently dated records from the Greenland GRIP, GISP2 and NGRIP ice cores for the past 104 ka reveal regional millennial-scale isotope gradients with possible Heinrich Event imprint. *Quat. Sci. Rev.* **106**, 29-46 (2014).
95. D. Lilien, A. *et al.*, Holocene Ice-Flow Speedup in the Vicinity of the South Pole. *Geophys. Res. Lett.* **45**, 6557-6565 (2018).
96. T. Blunier, J. Schwander, in *Physics of Ice Core Records,* T. Hondoh, Ed. (Hokkaido University Press, Sapporo, 2000), pp. 307-326.
97. P. Martinerie *et al.*, Air content paleo record in the Vostok ice core (Antarctica): A mixed record of climatic and glaciological parameters. *J. Geophys. Res.* **99**, 10565-10576 (1994).

98. E. Witrant *et al.*, A new multi-gas constrained model of trace gas non-homogeneous transport in firn: evaluation and behaviour at eleven polar sites. *Atmos. Chem. Phys.* **12**, 11465-11483 (2012).
99. M. W. Hörhold *et al.*, On the impact of impurities on the densification of polar firn. *Earth Planet. Sci. Lett.* **325–326**, 93-99 (2012).
100. J. Freitag, J. Kipfstuhl, T. Laepple, F. Wilhelms, Impurity-controlled densification: a new model for stratified polar firn. *J. Glaciol.* **59**, 1163-1169 (2013).
101. S. FUJITA *et al.*, Densification of layered firn in the ice sheet at Dome Fuji, Antarctica. *J. Glaciol.* **FirstView**, 1-21 (2016).
102. S. Fujita *et al.*, Densification of layered firn of the ice sheet at NEEM, Greenland. *J. Glaciol.* **60**, 905 (2014).
103. L. Arnaud, J. M. Barnola, P. Duval, in *Physics of Ice Core Records,* T. Hondoh, Ed. (2000), pp. 285-305.
104. F. Parrenin *et al.*, On the gas-ice depth difference (Δdepth) along the EPICA Dome C ice core. *Clim. Past* **8**, 1239-1255 (2012).
105. A. Landais *et al.*, Firn-air delta N-15 in modern polar sites and glacial-interglacial ice: a model-data mismatch during glacial periods in Antarctica? *Quat. Sci. Rev.* **25**, 49-62 (2006).
106. G. B. Dreyfus *et al.*, Firn processes and [delta]15N: potential for a gas-phase climate proxy. *Quat. Sci. Rev.* **29**, 28-42 (2010).
107. M. Guillevic *et al.*, Spatial gradients of temperature, accumulation and delta18O-ice in Greenland over a series of Dansgaard-Oeschger events. *Clim. Past* **9**, 1029-1051 (2013).
108. J. P. Severinghaus *et al.*, Deep air convection in the firn at a zero-accumulation site, central Antarctica. *Earth Planet. Sci. Lett.* **293**, 359-367 (2010).
109. C. Gordon *et al.*, The simulation of SST, sea ice extents and ocean heat transports in a version of the Hadley Centre coupled model without flux adjustments. *Clim. Dyn.* **16**, 147-168 (2000).
110. P. J. Valdes *et al.*, The BRIDGE HadCM3 family of climate models: HadCM3@ Bristol v1. 0. *Geoscientific Model Development* **10**, 3715-3743 (2017).
111. P. Braconnot *et al.*, Results of PMIP2 coupled simulations of the Mid-Holocene and Last Glacial Maximum - Part 2: feedbacks with emphasis on the location of the ITCZ and mid- and high latitudes heat budget. *Clim. Past* **3**, 279-296 (2007).
112. T. R. Jones *et al.*, Southern Hemisphere climate variability forced by Northern Hemisphere ice-sheet topography. *Nature* **554**, 351 (2018).
113. J. S. Singarayer, P. J. Valdes, P. Friedlingstein, S. Nelson, D. J. Beerling, Late Holocene methane rise caused by orbitally controlled increase in tropical sources. *Nature* **470**, 82-85 (2011).
114. C. D. Hewitt, A. J. Broccoli, J. F. Mitchell, R. J. Stouffer, A coupled model study of the last glacial maximum: Was part of the North Atlantic relatively warm? *Geophys. Res. Lett.* **28**, 1571-1574 (2001).
115. P. Braconnot *et al.*, Results of PMIP2 coupled simulations of the Mid-Holocene and Last Glacial Maximum - Part 1: experiments and large-scale features. *Clim. Past* **3**, 261-277 (2007).
116. A. Abe-Ouchi *et al.*, Ice-sheet configuration in the CMIP5/PMIP3 Last Glacial Maximum experiments. *Geosci. Model Dev.* **8**, 3621-3637 (2015).
117. H. Hasumi, S. Emori, K-1 coupled GCM (MIROC) description K-1 Technical Report No 1. *Center for Climate System Research*, (2004).
118. T. Obase, A. Abe-Ouchi, Abrupt Bølling-Allerød Warming Simulated under Gradual Forcing of the Last Deglaciation. *Geophys. Res. Lett.* **46**, 11397-11405 (2019).
119. A. Yamamoto *et al.*, Global deep ocean oxygenation by enhanced ventilation in the Southern Ocean under long-term global warming. *Global Biogeochemical Cycles* **29**, 1801-1815 (2015).

120. S. Sherriff-Tadano, A. Abe-Ouchi, Roles of Sea Ice–Surface Wind Feedback in Maintaining the Glacial Atlantic Meridional Overturning Circulation and Climate. *J. Clim.* **33**, 3001-3018 (2020).
121. M. A. Toscano, W. R. Peltier, R. Drummond, ICE-5G and ICE-6G models of postglacial relative sea-level history applied to the Holocene coral reef record of northeastern St Croix, U.S.V.I.: investigating the influence of rotational feedback on GIA processes at tropical latitudes. *Quat. Sci. Rev.* **30**, 3032-3042 (2011).
122. P. L. Whitehouse, M. J. Bentley, A. M. Le Brocq, A deglacial model for Antarctica: geological constraints and glaciological modelling as a basis for a new model of Antarctic glacial isostatic adjustment. *Quat. Sci. Rev.* **32**, 1-24 (2012).
123. D. Pollard, R. M. DeConto, Modelling West Antarctic ice sheet growth and collapse through the past five million years. *Nature* **458**, 329-332 (2009).
124. W. Peltier, Global glacial isostasy and the surface of the ice-age Earth: the ICE-5G (VM2) model and GRACE. *Annu. Rev. Earth Planet. Sci.* **32**, 111-149 (2004).
125. W. R. Peltier, D. Argus, R. Drummond, Space geodesy constrains ice age terminal deglaciation: The global ICE-6G_C (VM5a) model. *Journal of Geophysical Research: Solid Earth* **120**, 450-487 (2015).
126. J. W. Hurrell *et al.*, The Community Earth System Model: A Framework for Collaborative Research. *Bulletin of the American Meteorological Society* **94**, 1339-1360 (2013).
127. E. Brady *et al.*, The Connected Isotopic Water Cycle in the Community Earth System Model Version 1. *Journal of Advances in Modeling Earth Systems* **11**, 2547-2566 (2019).
128. E. C. Brady, B. L. Otto-Bliesner, J. E. Kay, N. Rosenbloom, Sensitivity to Glacial Forcing in the CCSM4. *J. Clim.* **26**, 1901-1925 (2013).
129. J. Zhu *et al.*, Reduced ENSO variability at the LGM revealed by an isotope-enabled Earth system model. *Geophys. Res. Lett.* **44**, 6984-6992 (2017).
130. K. E. Kohfeld *et al.*, Southern Hemisphere westerly wind changes during the Last Glacial Maximum: paleo-data synthesis. *Quat. Sci. Rev.* **68**, 76-95 (2013).
131. D. Noone, I. Simmonds, Annular variations in moisture transport mechanisms and the abundance of δ18O in Antarctic snow. *J. Geophys. Res.* **107**, 4742 (2002).
132. M. Werner, U. Mikolajewicz, M. Heimann, G. Hoffmann, Borehole versus isotope temperatures on Greenland: Seasonality does matter. *Geophys. Res. Lett.* **27**, 723-726 (2000).
133. G. A. Schmidt, G. Hoffmann, D. T. Shindell, Y. Hu, Modeling atmospheric stable water isotopes and the potential for constraining cloud processes and stratosphere-troposphere water exchange. *J. Geophys. Res.* **110**, (2005).
134. A. Touzeau *et al.*, Acquisition of isotopic composition for surface snow in East Antarctica and the links to climatic parameters. *The Cryosphere* **10**, 837-852 (2016).
135. J. Guan *et al.*, Understanding the temporal slope of the temperature-water isotope relation during the deglaciation using isoCAM3: The slope equation. *J. Geophys. Res.* **121**, 2016JD024955 (2016).
136. B. Stenni *et al.*, The deuterium excess records of EPICA Dome C and Dronning Maud Land ice cores (East Antarctica). *Quat. Sci. Rev.* **29**, 146-159 (2010).
137. M. Werner, M. Heimann, G. Hoffmann, Isotopic composition and origin of polar precipitation in present and glacial climate simulations. *Tellus* **53**, 53-71 (2001).
138. L. Sime, E. Wolff, K. Oliver, J. Tindall, Evidence for warmer interglacials in East Antarctic ice cores. *Nature* **462**, 342-345 (2009).
139. M. Kageyama *et al.*, The PMIP4-CMIP6 Last Glacial Maximum experiments: preliminary results and comparison with the PMIP3-CMIP5 simulations. *Clim. Past Discuss.* **2020**, 1-37 (2020).
140. V. Lipenkov, F. Candaudap, J. Ravoire, E. Dulac, D. Raynaud, A new device for the measurement of air content in polar ice. *J. Glaciol.* **41**, 423-429 (1995).

141. S. Sugawara, K. Kawamura, S. Aoki, T. Nakazawa, G. Hashida, Reconstruction of past variations of delta C-13 in atmospheric CO2 from its vertical distribution observed in the firn at Dome Fuji, Antarctica. *Tellus* **55**, 159-169 (2003).
142. P. Martinerie, V. Y. Lipenkov, D. Raynaud, Correction Of Air-content Measurements In Polar Ice For The Effect Of Cut Bubbles At The Surface Of The Sample. *J. Glaciol.* **36**, 299-303 (1990).
143. L. E. Mitchell *et al.*, Observing and modeling the influence of layering on bubble trapping in polar firn. *J. Geophys. Res.* **120**, 2014JD022766 (2015).
144. D. Raynaud, J. Chappellaz, C. Ritz, P. Martinerie, Air content along the Greenland Ice Core Project core: A record of surface climatic parameters and elevation in central Greenland. *J. Geophys. Res.-Oceans* **102**, 26607-26613 (1997).
145. J. M. Fegyveresi *et al.*, Five millennia of surface temperatures and ice-core bubble characteristics from the WAIS Divide deep core, West Antarctica. *Paleoceanography*, (2016).
146. O. Eicher *et al.*, Climatic and insolation control on the high-resolution total air content in the NGRIP ice core. *Clim. Past* **12**, 1979-1993 (2016).
147. J. O. Stone, Air pressure and cosmogenic isotope production. *J. Geophys. Res.-Solid Earth* **105**, 23753-23759 (2000).
148. A. Schilt *et al.*, Atmospheric nitrous oxide during the last 140,000 years. *Earth Planet. Sci. Lett.* **300**, 33-43 (2010).
149. J. P. Severinghaus, T. Sowers, E. J. Brook, R. B. Alley, M. L. Bender, Timing of abrupt climate change at the end of the Younger Dryas interval from thermally fractionated gases in polar ice. *Nature* **391**, 141-146 (1998).
150. F. Parrenin *et al.*, Synchronous Change of Atmospheric CO2 and Antarctic Temperature During the Last Deglacial Warming. *Science* **339**, 1060-1063 (2013).
151. K. Kawamura *et al.*, Convective mixing of air in firn at four polar sites. *Earth Planet. Sci. Lett.* **244**, 672-682 (2006).
152. G. Dreyfus, Princeton University, (2008).
153. J. P. Severinghaus, M. O. Battle, Fractionation of gases in polar ice during bubble close-off: New constraints from firn air Ne, Kr and Xe observations. *Earth Planet. Sci. Lett.* **244**, 474-500 (2006).
154. M. O. Battle *et al.*, Controls on the movement and composition of firn air at the West Antarctic Ice Sheet Divide. *Atmos. Chem. Phys.* **11**, 11007-11021 (2011).